Structure-property relationships and mobility optimization in sputtered La-doped $BaSnO_3$ films: Toward 100 $cm^2 V^{-1} s^{-1}$ mobility

William M. Postiglione, Koustav Ganguly, Hwanhui Yun, Jong Seok Jeong, Andrew Jacobson, Lindsey Borgeson, Bharat Jalan, K. Andre Mkhoyan, and Chris Leighton*

Department of Chemical Engineering and Materials Science, University of Minnesota, Minneapolis, Minnesota 55455, USA

(Received 18 January 2021; accepted 10 March 2021; published 13 April 2021)

The wide band gap semiconducting perovskite $BaSnO_3$ is of high current interest due to outstanding room temperature mobility at high electron density, fueled by potential applications in oxide, transparent, and power electronics. Due in part to a lack of lattice-matched substrates, $BaSnO_3$ thin films suffer from high defect densities, however, limiting electron mobility. Additionally, the vast majority of $BaSnO_3$ thin film research has focused on pulsed laser deposition or molecular beam epitaxy. Here, we present an exhaustive optimization of the mobility of $Ba_{0.98}La_{0.02}SnO_3$ films grown by a scalable, high-throughput method: high-pressure-oxygen sputter deposition. Considering target synthesis conditions, substrate selection, buffer layer structure, deposition temperature, deposition rate, thickness, and postdeposition annealing conditions, and by combining high-resolution x-ray diffraction, reciprocal space mapping, rocking curve analysis, scanning transmission electron microscopy, atomic force microscopy, and temperature-dependent electronic transport measurements, detailed understanding of synthesis-structure-property relationships is attained. Optimized room temperature mobility of 96 $cm^2 V^{-1} s^{-1}$ is achieved in vacuum-annealed $GdScO_3$(110)/$BaSnO_3$(120 nm)/$Ba_{0.98}La_{0.02}SnO_3$(200 nm) heterostructures, as well as 92 $cm^2 V^{-1} s^{-1}$ on unbuffered substrates and 87 $cm^2 V^{-1} s^{-1}$ without postdeposition annealing. These results, including important trends in defect densities and a surprising dependence of mobility on lattice mismatch, substantially expand the understanding of the interplay between deposition conditions, microstructure, and transport in doped $BaSnO_3$ films, establishing competitive mobilities in films fabricated via a scalable, high-throughput, industry-standard technique.

DOI: 10.1103/PhysRevMaterials.5.044604

I. INTRODUCTION

The discovery of room temperature electron mobility $>300\,cm^2 V^{-1} s^{-1}$ in *n*-doped single crystal $BaSnO_3$ (BSO) [1–3] triggered intense investigation of this wide band gap (∼3 eV) semiconducting perovskite. Such outstanding room temperature mobility in this perovskite oxide, combined with its wide gap, high visible transparency, and retention of high mobility (μ) to exceptional electron density (n), suggests potential for applications in oxide, transparent, and power electronics [4–14]. *n*-type doping of BSO has been demonstrated with both substitutional (e.g., La_{Ba} [1–3,6,8–11,13–40], Pr_{Ba} [15–18], Nd_{Ba} [15,18,41], Gd_{Ba} [17,18], Sb_{Sn} [42–45]) and vacancy (V_O [12,15,16,46,47]) dopants, La doping (i.e., in $Ba_{1-x}La_xSnO_3$, or "BSO:La") proving particularly effective (up to $\sim 10^{21}$ cm^{-3}) [1–3,6,8–11,13–40]. The exceptional ambient mobility is thought to originate from low electron effective mass (m_e^*) due to the dispersive Sn-5*s*-dominated conduction band [2,32,48–51], along with low longitudinal optical phonon scattering rate [13,52]. BSO also possesses a relatively large dielectric constant (∼20) [53–55], minimizing ionized impurity scattering.

The potential of BSO for heterostructures and devices has of course driven interest in thin films, particularly epitaxial films, which have been heavily studied via pulsed laser deposition (PLD [1,2,8,17–33,39,41,42,44,45,56]) and molecular beam epitaxy (MBE [6,9,11,13,36,38,55,57,58]). While progress has been rapid [1,2,6,8–14,17–39,41,42,44–47,56,57,59], substantial challenges persist, particularly due to the lack of commercially available lattice-matched substrates around the 4.116 Å BSO cubic lattice parameter. Common perovskite substrate materials such as $LaAlO_3$ (LAO), $(LaAlO_3)_{0.3}(Sr_2AlTaO_6)_{0.7}$ (LSAT), and $SrTiO_3$ (STO) present compressive lattice mismatches of −8.6, −6.4, and −5.4%, respectively, and even scandate substrates such as $GdScO_3$ (GSO) and $PrScO_3$ (PSO) have −3.9 and −2.2% mismatch. Alternatively, rock-salt substrates like MgO offer moderate tensile mismatch of +2.3%, but with structure and symmetry mismatch with perovskite BSO. Growth of BSO on these substrates thus results in low critical thickness for strain relaxation, typically relaxed films, high densities of misfit and threading dislocations (MDs and TDs), and even low-angle grain boundaries (LAGBs) [1,2,6,11–13,18,19,25–28,31,37,38,45,46,60]. Other factors, such as challenges with stoichiometry and phase control, and charged impurity incorporation, lead to further defects, including nonstoichiometry-accommodating point defects, stacking faults, deep acceptors, etc. [6,13,33,37,38,50,61,62]. These charged defects efficiently compensate donors in lightly *n*-doped BSO, prominently impact $\mu(n)$, and limit the peak

*leighton@umn.edu

mobility in films [1,2,11–13,25–27,37,45]. While the accessible n range is limited to $>10^{17}$ cm^{-3}, μ increases significantly with n (up to $\sim 10^{20}$ cm^{-3}) before decreasing at the highest n [1,2,11–13,25–27,37,45]. In conventionally doped films, μ is therefore understood to be limited by charged dislocation scattering at low n, then ionized impurity scattering at the highest n [1,2,5,11–13,25–28,37,45,52,63]. Similarly, in electrolyte-gated BSO films, charged dislocations are thought to limit μ at low n, followed by electrolyte-induced and surface/interface scattering at the highest n [14,56,58].

Based on the above, various strategies have been employed to improve μ in n-doped BSO films, including refinement of deposition parameters [20,22,25,41,46,47], application of perovskite substrates with minimized lattice mismatch [11,16,30,31,33,36,37,40,58,64,65], incorporation of undoped buffer layers to decrease TD densities in overlying doped layers [6,13,26,27,31,37–39] (or growth of very thick doped films [13,18–23,28,32,39,41]), adsorption-controlled MBE for improved stoichiometry control [6,11,13,36–38,57], very high-temperature growth [31], and postdeposition thermal treatments [21,23,24,29]. The latter have developed rapidly in recent years, with annealing, particularly under reducing conditions, being shown capable of substantial mobility enhancements [21,23,24]. Mobilities have been improved from 41 to 78 cm^2 V^{-1} s^{-1} [24], 74 to 102 cm^2 V^{-1} s^{-1} [21], and 16 to 122 cm^2 V^{-1} s^{-1} [23], for example, using conditions such as 1000 °C in N_2, 725 °C in vacuum, and 950 °C in damp 0.5% H_2/N_2, respectively. Refinement of temperature and O_2 partial pressure has also been employed [21,23], accompanying structural characterization revealing improvement of various microstructural parameters, including in-plane grain size [21,23,24]. Several mechanisms for the annealing-induced mobility improvement have been advanced, including improved screening of charged impurities by V_O doping [21,23]; agglomeration of V_O around TDs and LAGBs, thus screening and/or neutralizing these charged defects [21]; and V_O-facilitated in-plane grain growth and TD annihilation [21,23,24].

Such efforts have realized room temperature BSO film mobilities of 120−183 cm^2 V^{-1} s^{-1} by MBE [6,11,13,37] and up to 140 cm^2 V^{-1} s^{-1} by PLD [31]. While these growth methods are powerful, particularly for oxides, it is nevertheless important to explore other deposition methods. Given the application potential of BSO, scalable, high-throughput methods are of special interest. Sputter deposition is attractive in this context, being a widely employed, industry-standard, highly scalable film deposition technique [66]. Studies of sputtered BSO are limited, however, with reported mobilities spanning 11 cm^2 V^{-1} s^{-1} [59] to 22 cm^2 V^{-1} s^{-1} [12,46] in V_O-doped films, and from 9 cm^2 V^{-1} s^{-1} [35] to 21 cm^2 V^{-1} s^{-1} [34] to 30 cm^2 V^{-1} s^{-1} [14,58] in La-doped films, the latter value perhaps being the largest reported to date. It is thus unclear whether mobility in sputtered BSO could ever be competitive with PLD- and MBE-grown material. Comprehensive mobility optimization of a model system such as BSO:La by sputter deposition would also be broadly instructive in terms of establishing interrelationships between deposition parameters, microstructure, and electronic transport via another growth method. Indeed, despite the substantial literature on doped BSO films, few studies have elucidated the impacts of multiple deposition parameters, particularly when coupled with broad structural and electronic characterization.

In light of the above, we present here an exhaustive study of the interrelationships between deposition conditions, microstructure, and electronic transport in BSO:La thin films grown by high-pressure-oxygen sputter deposition. Epitaxial $Ba_{0.98}La_{0.02}SnO_3$ films are studied as a function of sputter target synthesis conditions, substrate choice (perovskite and nonperovskite, thus probing both lattice and symmetry mismatch), deposition temperature, thickness, deposition rate, postdeposition vacuum annealing, and buffer layer structure and thickness. Temperature-dependent resistivity (ρ), Hall electron density, and mobility measurements are then combined with structural characterization via high-resolution wide-angle x-ray diffraction (WAXRD), rocking curve (RC) analysis, reciprocal space mapping (RSM), cross-sectional and plan-view scanning transmission electron microscopy (STEM), and atomic force microscopy (AFM), to accrue detailed understanding of synthesis-structure-property relationships, particularly via trends in defect densities. We also highlight a surprising relationship between mobility and lattice mismatch. The mobility of sputtered BSO:La is thus optimized, achieving 96 cm^2 V^{-1} s^{-1} in annealed and buffered films, 92 cm^2 V^{-1} s^{-1} in unbuffered films, and 87 cm^2 V^{-1} s^{-1} without postdeposition annealing. This brings sputtered BSO to comparable electronic quality with PLD-grown material, suggesting that $>$ 100 cm^2 V^{-1} s^{-1} is very likely within reach with this scalable, high-throughput, industry-standard deposition method. More generally, the structure-property relationship understanding hereby developed will be of broad utility for the community studying thin film $BaSnO_3$ and related oxides.

II. EXPERIMENTAL DETAILS

BSO:La films were synthesized by high-pressure-oxygen sputtering, a variant of sputter deposition that employs pure O_2, with no additional inert gas, at pressures ∼1–3 Torr. The essential concept is to mitigate negative-ion-induced resputtering by thermalizing reactive oxygen ions in a dense, high-pressure plasma, thus enabling low-energy growth of low-defect-density films from compound targets at short source-to-substrate distances in an on-axis geometry [67]. The resulting deposition rates are generally improved over more conventional (∼100 mTorr, off axis) reactive sputtering techniques. This technique has proven effective for the growth of high-quality epitaxial oxide films at elevated substrate temperatures, encompassing high-temperature superconducting cuprates [67–71], perovskite manganites [71–73], perovskite cobaltites [74–76], $SrTiO_3$ [72,73,77], etc., even achieving highly stoichiometric growth under homoepitaxial conditions [77].

For the current studies, 2 inch diameter ceramic $Ba_{1-x}La_xSnO_3$ (BSO:La) sputtering targets were synthesized by solid state reaction, cold pressing, and sintering. Consistent with many BSO studies, $x = 0.02$ was targeted as a representative doping level, corresponding to $n \approx 3 \times 10^{20}$ cm^{-3},

assuming full dopant activation and negligible compensation. Briefly, stoichiometric amounts of La_2O_3 (99.99%), $BaCO_3$ (99.98%), and SnO_2 (99.9%) were dried, hot weighed, ground, and reacted at 1200 °C for 24 h in air. Grinding and reaction were performed three times, until powder x-ray diffraction (PXRD) indicated phase purity. Powders were then cold pressed at 275 MPa and sintered at temperatures (T_{sinter}) between 1350 and 1550 °C in air, with warming and cooling rates of 0.5 °C min^{-1}. Epitaxial BSO:La films were grown from these targets by high-pressure-oxygen sputtering at direct current (dc) powers of 20–60 W, high purity (99.998%) O_2 pressure (P_{O2}) of 1.9 Torr, deposition temperatures (T_{dep}) of 750–900 °C, and deposition rates (R) of 0.1–1.2 nm min^{-1} (controlled primarily by dc current). Typical source-to-substrate distances in this form of high-pressure-oxygen sputtering are very short, e.g., 10–20 mm. $SrLaAlO_4$(SLAO)(001), LAO(001), LSAT(001), STO(001), GSO(110), PSO(110), and MgO(001) substrates were employed and were annealed at 900 °C for 15 min in P_{O2} = 1.9 Torr before deposition. Immediately after growth, P_{O2} was increased to >150 Torr for cooling. Postgrowth vacuum annealing, when performed, employed a tube furnace at 500–800 °C and $\sim 6 \times 10^{-7}$ Torr, using 5 °C min^{-1} heating and cooling rates.

Reagent powders and targets were characterized by PXRD in a Rigaku Miniflex 600 with Cu K_α radiation, and by energy dispersive x-ray spectroscopy (EDS) in a JEOL JSM-6010PLUS/LA scanning electron microscope. BSO:La films were characterized by high-resolution WAXRD, x-ray RC analysis, RSM, contact-mode AFM, and cross-sectional and plan-view STEM. WAXRD, RC, and RSM characterizations were done in Panalytical X'Pert Pro and Rigaku Smartlab XE systems, using Cu K_α radiation. WAXRD Laue fringes were typically used for film thickness determination, along with grazing-incidence x-ray reflectivity in cases where Laue fringes were absent. Cross-sectional STEM samples were prepared by a focused ion beam (FIB) lift-out method using a FEI Helios Nanolab G4 dual-beam FIB. Samples were thinned using a 30 kV Ga ion beam and further polished using a 2 kV Ga ion beam to minimize damaged layers at the surface. The thickness of the cross-sectional specimens was in the 35–60 nm range, estimated via the electron energy loss spectroscopy log-ratio method [78]. Plan-view STEM samples were prepared by mechanical wedge polishing using Multiprep (Allied High Tech Products, Inc.). STEM images were obtained using an aberration-corrected FEI Titan G2 60–300 STEM operated at 200 keV with ~30 pA beam current. The convergent semi-angle of the incident STEM probe was 17 mrad, and the annular dark-field (ADF) detector inner angles were 19 and 55–93 mrad for low-angle ADF (LAADF) and high-angle ADF (HAADF) images, respectively. Contact-mode AFM employed a Bruker Nanoscope V Multimode 8. Electronic transport measurements were performed with dc excitation in a four wire van der Pauw configuration in a Quantum Design Physical Property Measurement System (PPMS) at temperatures (T) from 1.8–300 K and magnetic fields up to 9 T. Either soldered In or sputtered Pt(200 nm) contacts were used (the latter specifically for annealing studies), and checks were made for non-Ohmicity and self-heating.

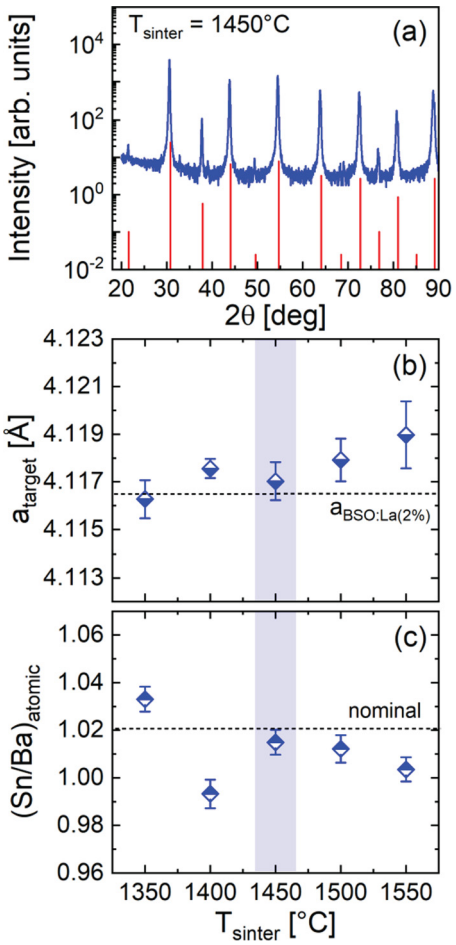

FIG. 1. Representative powder x-ray diffraction pattern (blue) from a bulk polycrystalline $La_{0.02}Ba_{0.98}SnO_3$ (BSO:La) target sintered at 1450 °C. The red vertical lines depict the reference pattern [3]. (b) and (c) Sintering temperature (T_{sinter}) dependence of the sputtering target lattice parameter (a_{target}) and energy dispersive spectroscopy (EDS) Sn:Ba atomic ratio. The horizontal dotted lines are bulk literature values for polycrystalline $La_{0.02}Ba_{0.98}SnO_3$ [2]. Blue shaded regions indicate the deduced optimal $T_{sinter} \approx 1450$ °C. Error bars in (b) represent standard errors on the intercepts of linear regressions of a_{target} vs $\cos^2(\theta_{hkl})/\sin(\theta_{hkl})$. Error bars in (c) represent standard deviations of Sn and Ba atomic percentages from EDS.

III. RESULTS AND ANALYSIS

A. Sputtering target synthesis

Shown in Fig. 1(a) is a representative PXRD pattern from a BSO:La sputtering target synthesized by the abovementioned process at $T_{sinter} = 1450$ °C. Such targets are phase pure within the detection limits of lab PXRD, each observed reflection being consistent with the standard reference pattern (red). This was true at all T_{sinter} above 1400 °C, lower T_{sinter} resulting in some residual BaO and SnO_2. As shown in Fig. 1(b), the extracted cubic lattice parameter (a_{target}) varies with T_{sinter}, comparison with the $Ba_{0.98}La_{0.02}SnO_3$ bulk value (horizontal dotted line) [2] revealing expanded a_{target} at high T_{sinter}. This is further elucidated in Fig. 1(c), which plots the T_{sinter} dependence of the Sn/Ba atomic ratio [$(Sn/Ba)_{atomic}$] from EDS measurements on these bulk targets. Aside from an

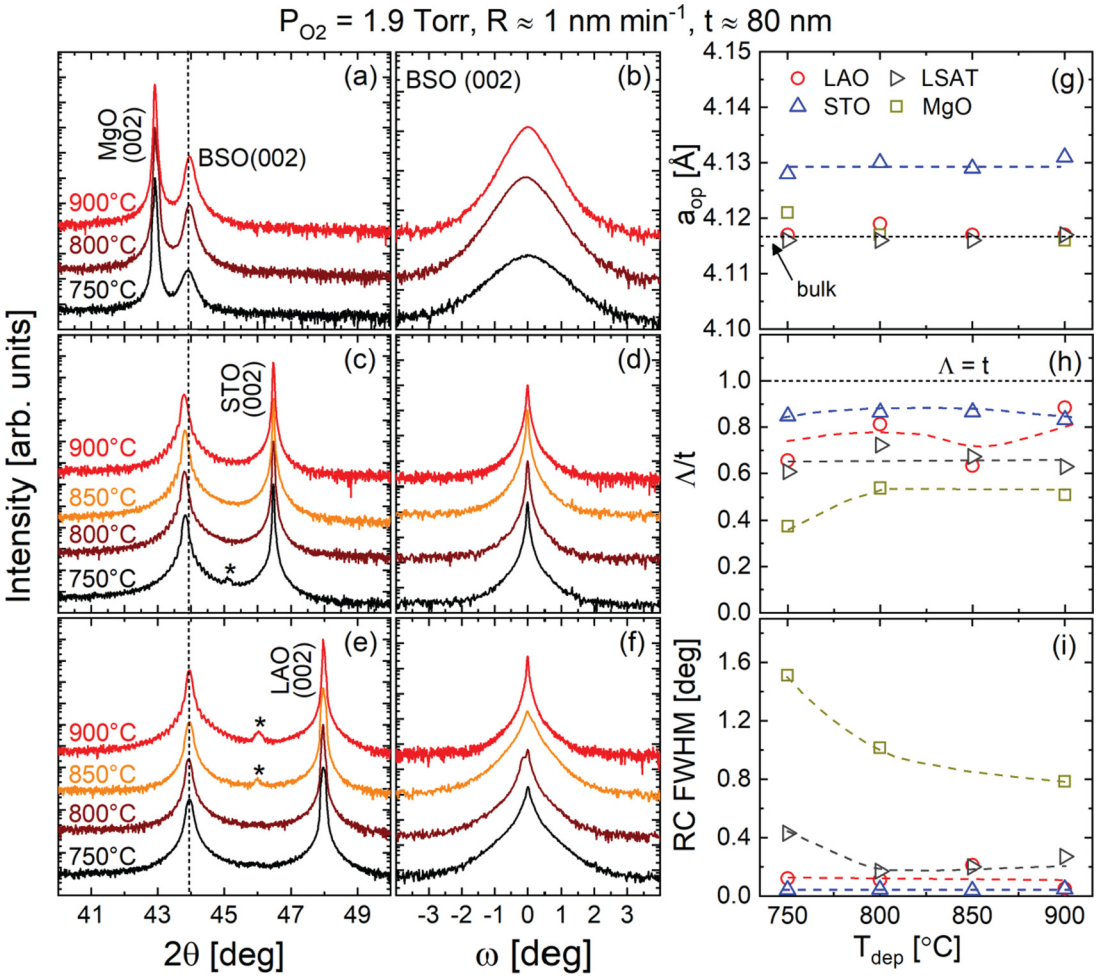

FIG. 2. (a), (c), and (e) High-resolution wide-angle specular x-ray diffraction around the 002 film and substrate reflections and (b), (d), and (f) corresponding 002 film rocking curves, from $La_{0.02}Ba_{0.98}SnO_3$ (BSO:La) films sputtered at varied deposition temperature (T_{dep}). Data are offset for clarity and are shown on MgO, $SrTiO_3$ (STO), and $LaAlO_3$ (LAO) substrates. Oxygen pressure (P_{O2}), deposition rate (R), and thickness (t) were held constant at 1.9 Torr, ∼1 nm min^{-1}, and ∼80 nm, respectively. The vertical black dotted line in (a), (c), and (e) corresponds to the bulk lattice parameter. Small peaks marked with an asterisk are hybrid reflections [84]. T_{dep} dependence of (g) the out-of-plane lattice parameter (a_{op}), (h) the Scherrer length-to-thickness ratio (Λ/t), and (i) the 002 film rocking curve full width at half maximum (RC FWHM) on MgO, STO, LAO, and $(LaAlO_3)_{0.3}(Sr_2TaAlO_6)_{0.7}$ LSAT substrates. The horizontal black dotted lines in (g) and (h) mark the bulk lattice parameter and $\Lambda = t$, respectively. The colored dashed lines in (g), (h), and (i) are guides to the eye.

outlier at 1400 °C {where a_{target} may also be slightly anomalous [Fig. 1(b)]}, $(Sn/Ba)_{atomic}$ generally decreases with increasing T_{sinter}, potentially reflecting Sn loss associated with Sn oxide volatility [16]. The concomitant lattice expansion at high T_{sinter} could then be interpreted in terms of increased density of nonstoichiometry-accommodating defects. On the basis of Figs. 1(b) and 1(c), $T_{sinter} = 1450$ °C (blue shaded region) was thus selected for film deposition due to the close correspondence of a_{target} and $(Sn/Ba)_{atomic}$ to their nominal bulk values.

B. Influence of deposition temperature

Sputtering targets synthesized under these optimized conditions were subsequently used for sputter deposition of BSO:La films. Presented in Fig. 2 is the evolution of the structural and microstructural information from high-resolution WAXRD as T_{dep} is varied up to the practical limit of the employed deposition system (900 °C). In these initial experiments, the film thickness (t) was held constant at a representative ∼80 nm, R was fixed at a moderate ∼1 nm min^{-1} (controlled by the sputtering current, and thus dc power), and P_{O2} was set to 1.9 Torr, a typical value in the high-pressure-oxygen sputter deposition stability window. (A prior paper showed negligible sensitivity of undoped BSO structural parameters to P_{O2} [46]). Figures 2(a), 2(c), and 2(e) show high-resolution specular WAXRD scans (intensity vs 2θ) around the 002 reflections of BSO:La films grown on representative MgO, STO, and LAO substrates, respectively. No buffer layer was employed in these initial studies. On LAO [Fig. 2(e)], the BSO:La reflection is seen to align perfectly with the bulk lattice parameter of the sputtering target (4.117 Å), the only change with increasing T_{dep} being the onset of visible Laue fringes, pointing to decreased roughness. A similar trend occurs on STO [Fig. 2(c)], although with a systematic peak shift to lower 2θ, i.e., expanded out-of-plane

lattice parameter. On MgO, however, the situation is different; no Laue fringes occur, and the noticeably broader film peak sharpens at higher T_{dep}.

The above trends are illustrated more clearly in Figs. 2(g) and 2(h), which plot the T_{dep} dependence of the extracted out-of-plane lattice parameter (a_{op}) and Scherrer length-to-thickness ratio (Λ/t). (The latter is simply the length scale extracted from applying the Scherrer equation to the observed 2θ peak width, normalized to t.) In these ∼80 nm films, a_{op} on MgO, LAO, and also LSAT [not shown in Figs. 2(a), 2(c), and 2(e)] varies negligibly from bulk (horizontal dotted line), confirming fully relaxed films, consistent with the low critical thickness expected from the large lattice mismatches. This close correspondence with the bulk lattice parameter also implies relatively low concentrations of nonstoichiometry-accommodating point defects, suggesting good stoichiometry preservation under these growth conditions. The a_{op} on STO substrates [Fig. 2(g)] is clearly anomalous, however, exhibiting a constant ∼0.01 Å expansion. The origin of this is unclear, although it has been observed before in STO/BSO films [2,17,18,57], some form of interdiffusion being one possible explanation. Turning to Λ/t in Fig. 2(h), two additional conclusions are apparent. First, in all cases, these ∼80 nm thick BSO:La films exhibit $\Lambda/t < 1$, meaning that full structural coherence through the film thickness is not achieved. This is unsurprising in relaxed films (which necessarily exhibit microstrain contributions to the 2θ peak width in specular WAXRD, thus decreasing Λ/t from 1), although the deviations from unity are substantial here. Second, while Λ/t on the perovskite substrates is 0.6–0.9, independent of T_{dep}, growth on MgO results in lower Λ/t, increasing with T_{dep}. The through-thickness structural coherence is thus poorer on MgO than perovskite substrates (even those with higher lattice mismatch), emphasizing the effects of structure and symmetry mismatch.

Figures 2(b), 2(d), and 2(f) show corresponding x-ray RCs through the 002 BSO:La reflections, which reveal complementary trends with substrate and T_{dep}. On the perovskite substrates STO and LAO [Figs. 2(d) and 2(f)], relatively narrow RCs are found, with only minor apparent variations with T_{dep}. On MgO, on the other hand, much broader RCs occur, narrowing distinctly with increasing T_{dep}. These trends are shown more clearly in Fig. 2(i), which plots the RC full width at half maximum (FWHM) vs T_{dep}. The RC width on perovskite substrates is seen to be generally low (reaching 0.04 ° on STO, for example), while growth on MgO results in ∼0.8 ° RC width even at $T_{dep} = 900\,^{\circ}$C. Like the trends in out-of-plane structural coherence in Fig. 2(h), BSO:La films on lattice- and symmetry-mismatched MgO thus exhibit significant mosaic spread, decreasing with T_{dep}. One simple interpretation of this is decreasing TD density with increasing T_{dep}, as returned to below.

The impact of these T_{dep}-dependent structural and microstructural trends on electronic transport is illustrated in Fig. 3. Figures 3(a)–3(c) show the T_{dep} dependence of the 300 K ρ, n, and μ, respectively, the horizontal dotted line in (b) marking the n value corresponding to the nominal $x = 0.02$ doping. The Hall electron density matches this value closely at $T_{dep} \geqslant 800\,^{\circ}$C, indicating essentially full dopant activation and negligible compensation in these ∼80 nm thick

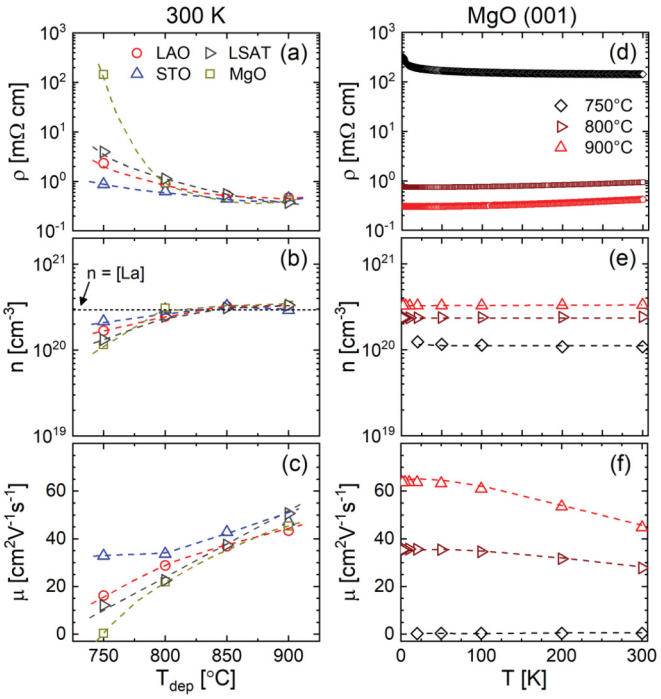

FIG. 3. Deposition temperature (T_{dep}) dependence of the 300 K (a) resistivity (ρ), (b) Hall electron density (n), and (c) Hall mobility (μ) for $La_{0.02}Ba_{0.98}SnO_3$ (BSO:La) films on MgO, $LaAlO_3$ (LAO), $SrTiO_3$ (STO), and $(LaAlO_3)_{0.3}(Sr_2TaAlO_6)_{0.7}$ (LSAT) substrates. Oxygen pressure, deposition rate, and thickness were held constant at 1.9 Torr, ∼1 nm min^{-1}, and ∼80 nm, respectively. Temperature dependence of (d) ρ, (e) n, and (f) μ for the films on MgO in (a), (b), and (c), respectively. The horizontal black dotted line in (b) marks the nominal n for full dopant activation. Colored dashed lines are guides to the eye.

films. Decreasing T_{dep} to 750 °C, however, leads to n significantly below nominal, likely due to nonnegligible densities of compensating defects at lower T_{dep}. As shown in Fig. 3(c), related effects occur in scattering also, μ(300 K) generally decreasing with decreasing T_{dep}. This effect is significant, μ(300 K) falling from 43−53 cm^2 V^{-1} s^{-1} at $T_{dep} = 900\,^{\circ}$C, to below 33 cm^2 V^{-1} s^{-1} at 750 °C (in some cases far below). Two additional trends can be seen in Fig. 3(c). First, at $T_{dep} \geqslant 800\,^{\circ}$C, quite similar μ(300 K) occurs on all substrates (LAO, LSAT, STO, and MgO), i.e., μ is only weakly dependent on lattice mismatch. In such relaxed $t \approx 80$ nm films, the density of defects that impact scattering is thus apparently only weakly dependent on lattice mismatch. This is clarified below, where it is shown from STEM that larger MD densities at higher film-substrate lattice mismatch do not lead to dramatically higher densities of TDs or LAGBs in thick, relaxed films. The second trend apparent in Fig. 3(c) is that the weak sensitivity of mobility to substrate breaks down at the lowest T_{dep}, where μ(300 K) on MgO falls far beneath the perovskite substrates, consistent with the structural trends in Figs. 2(h) and 2(i). For completeness, Fig. 3(a) then plots the ρ(300 K) that results from Figs. 3(b) and 3(c), showing the expected decrease with increasing T_{dep} and much higher ρ(300 K) on MgO at low T_{dep}. As a final comment on Figs. 3(a)–3(c), note that μ(300 K) shows no saturation at the highest T_{dep} of 900 °C, suggesting

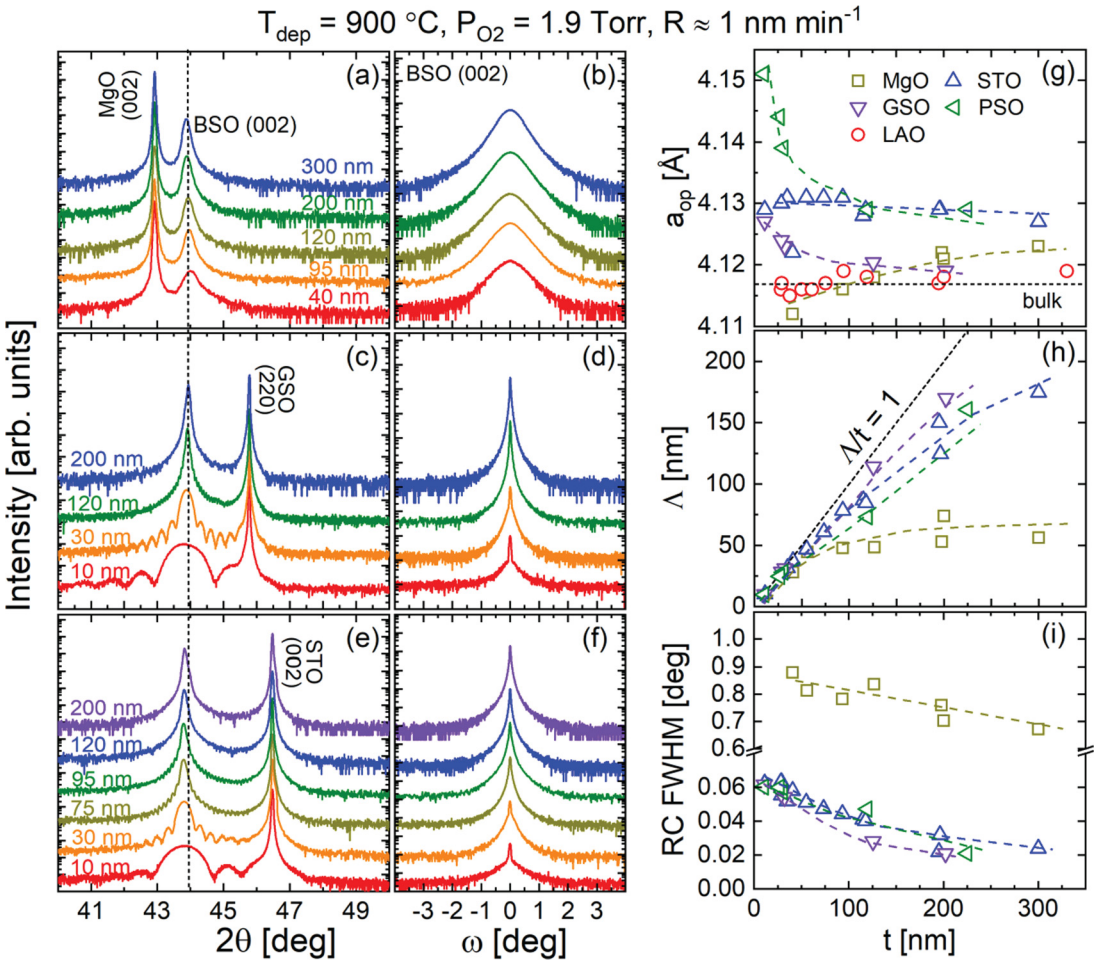

FIG. 4. (a), (c), and (e) High-resolution wide-angle specular x-ray diffraction around the 002 film and 002/220 substrate reflections and (b), (d), and (f) corresponding 002 film rocking curves, from $La_{0.02}Ba_{0.98}SnO_3$ (BSO:La) films with various thickness (t). Data are offset for clarity and are shown on MgO, $GdScO_3$ (GSO), and $SrTiO_3$ (STO) substrates. Deposition temperature (T_{dep}), oxygen pressure (P_{O2}), and deposition rate (R) were held constant at 900 °C, 1.9 Torr, and ∼1 nm min^{-1}, respectively. The vertical black dotted line in (a), (c), and (e) corresponds to the bulk lattice parameter. t dependence of (g) the out-of-plane lattice parameter (a_{op}), (h) the Scherrer length (Λ), and (i) the 002 film rocking curve full width at half maximum (RC FWHM) on MgO, STO, GSO, $PrScO_3$ (PSO), and $LaAlO_3$ (LAO) substrates (note the break on the RC FWHM axis). The black dotted lines in (g) and (h) mark the bulk lattice parameter and $\Lambda = t$, respectively. The colored dashed lines in (g), (h), and (i) are guides to the eye.

that postdeposition thermal annealing could be beneficial; this is explored in Sec. III E.

Using MgO substrates as a representative example, where variations with T_{dep} are strongest, Figs. 3(d)–3(f) then show the T dependence of ρ, n, and μ, respectively, at various T_{dep}. In all cases, including $T_{dep} = 750$ °C, where significant compensation arises, $n(T)$ [Fig. 3(e)] is remarkably flat, indicating the degenerate doping that would be expected from the high x and shallow nature of the La_{Ba} dopants [50,62]. Consistent with Fig. 3(c), $\mu(T)$ in Fig. 3(f) varies strongly with T_{dep}, from very low values that decrease on cooling [not visible in Fig. 3(f)], to values of 45 cm^2 V^{-1} s^{-1} that increase to 65 cm^2 V^{-1} s^{-1} on cooling, indicating phonon-limited mobility. The resulting $\rho(T)$ curves in Fig. 3(d) are relatively weakly T dependent, crossing from negative low temperature $d\rho/dT$ at $T_{dep} = 750$ °C (due to weak localization [79]), to positive $d\rho/dT$ across the entire T range at higher T_{dep}. At this high doping level and thickness, metallic transport is thus evident, consistent with (the T independent) n substantially exceeding the critical value for the insulator-metal transition. The latter was found to lie in the 10^{18} cm^{-3} range in our prior paper on V_O-doped BSO [12].

C. Influence of film thickness

Based on the results in Sec. III B, T_{dep} was next fixed at our maximum value of 900 °C, P_{O2} was held at 1.9 Torr, R was held at 1 nm min^{-1}, and t was varied from 10–300 nm. Analogous to Fig. 2, Figs. 4(a)–4(f) show specular WAXRD scans around the 002 film reflections, along with corresponding RCs, this time on representative MgO (top), GSO (middle), and STO (bottom) substrates. Considering films on STO first, WAXRD [Fig. 4(e)] reveals no visible change in a_{op} with t from 10 to 200 nm, although the anomalous lattice expansion persists (see the constant shift to the left of the vertical dotted line corresponding to the bulk lattice parameter). A clear decrease in 2θ peak width does occur with increasing t, however, indicating increasing Λ. Laue fringes are also obvious

at low t, but gradually fade with increasing t, likely due to both resolution limitations and a gradual increase in film surface roughness. As shown in the Supplemental Material [80] (Fig. S1), AFM indicates RMS surface roughnesses of ∼1 nm at $t = 200$ nm. Similar behavior to Fig. 4(e) occurs on GSO [Fig. 4(c)], both in terms of peak width and Laue fringes, but with a clear evolution in the 002 peak position, from distinctly to the left of the vertical dotted line at low t to close to it at 200 nm. As discussed further below, this suggests strain relaxation on this relatively low lattice mismatch perovskite substrate. On MgO, on the other hand [Fig. 4(a)], no Laue fringes are seen at any t, the 002 reflection again occurring close to the expected bulk position, this time with little variation in peak width. Moving to Figs. 4(b), 4(d), and 4(f), the trends in RCs can be seen to be similar for the two perovskite substrates [Figs. 4(d) and 4(f)], where two component curves at low t (i.e., sharp peaks on a broader hump, likely related to strained and relaxed film regions [81]) evolve into single peaks at higher t. In contrast, on MgO, consistent with Fig. 2(b), much broader RCs occur, with a clear width reduction with increasing t.

These trends are shown more clearly in Figs. 4(g)–4(i), which plot the t dependence of a_{op}, Λ, and the RC FWHM, respectively, the horizontal dotted line in (g) marking the bulk lattice parameter, and the dotted line in (h) corresponding to $\Lambda = t$. From Fig. 4(g), the a_{op} on MgO, LAO, and STO is relatively t independent, except for a small expansion at high t on MgO (potentially indicating some degree of nonstoichiometry at high t). The t independence on these substrates indicates essentially relaxed behavior in this t range, consistent with a very low critical thickness for strain relaxation at these large (up to −8.6%) lattice mismatches. This critical thickness was found to be <10 nm in a prior paper on sputtered STO/BSO, for example [46]. On PSO, however, and to a lesser extent GSO, where the lattice mismatches are −2.2 and −3.9%, respectively, a clear evolution occurs from much larger a_{op} at low t to bulklike a_{op} at high t. This is strong evidence of t-dependent strain relaxation, the compressive in-plane lattice mismatch leading to expanded a_{op} at low t that gradually relaxes with t. This is supported by the asymmetric 103 RSM in Fig. S2 in the Supplemental Material [80], where a 10 nm thick film on PSO is verified to be essentially fully strained, i.e., pseudomorphic with the substrate. From Fig. 4(g), the strain relaxation is essentially complete by 200 nm on GSO but may persist over the entire probed t range on PSO.

Figure 4(h) reveals related trends to Fig. 2(h). Specifically, $\Lambda = t$ is found at low t (<50 nm) on all substrates, giving way at higher t to behavior where the values on MgO saturate at ∼50–75 nm, while no such saturation occurs on perovskite substrates, which yield consistently higher Λ. Again, this indicates diminished structural coherence on the structure- and symmetry-mismatched MgO substrate in comparison to the structure- and symmetry-matched (but lattice mismatched) perovskites. Moving to the RC FWHM, Fig. 4(i) then shows a continuous decrease with t on all substrates (reaching 0.02° on GSO, for example), but again with substantially larger magnitude on MgO [note the break on the FWHM axis in Fig. 4(i)]. The mosaic spread is thus apparently much larger on MgO than perovskite substrates (likely indicating higher TD densities), with all substrates yielding decreases with t to the highest values probed (300 nm), suggesting slow but gradual mitigation of TD density with increasing t [13,18–20,22,41].

To strengthen conclusions regarding MD and TD densities and to provide complementary real-space characterization of these BSO:La films, cross-sectional and plan-view STEM imaging was performed. This was done on 200 nm thick unbuffered BSO:La films grown on LAO, STO, GSO, and PSO substrates, at $T_{dep} = 900\,^{\circ}$C and $R \approx 1$ nm min^{-1}, enabling direct comparison with Fig. 4. As shown in Fig. 5(a), HAADF cross-sectional STEM images (top panels) reveal relatively smooth, dense films on all substrates, but with weak, yet clearly visible, vertical striations. The origin of the latter is clarified by the corresponding LAADF images [Fig. 5(a), bottom panels], where the enhanced strain contrast reveals columnar grains, with in-plane grain size of ∼30 nm under these conditions [roughly consistent with AFM (see Fig. S1 [80])]. As reported previously, such features indicate LAGBs, with extents of in-plane twist and out-of-plane tilt that have been characterized with various TEM methods and reconciled with RC and in-plane WAXRD peak widths [60]. Important in the current context, it is seen from Fig. 5(a) that the in-plane grain size exhibits little variation with lattice mismatch, from −8.6% on LAO to −2.2% on PSO. Equivalent plan-view HAADF and LAADF STEM images are shown in the left and right panels of Fig. 5(b), respectively, on representative LAO and PSO substrates. These images, particularly the LAADF ones, reveal the expected contrast associated with the in-plane grains (∼30 nm grain size) as well as a small density of highly strained regions (marked with yellow arrows). The latter could be associated with screw dislocations or anomalously highly misoriented grains. The bright white regions in the LAADF images in Fig. 5(b) (green arrows), on the other hand, likely occur at regions where a columnar grain fails to penetrate the entire thickness, as can be seen in the equivalent LAADF cross-sectional images in Fig. 5(a). Close inspection of the plan-view LAADF images in Fig. 5(b) also enables identification and quantification of edge-character TDs, which are marked with yellow dots. As shown in the insets, in some regions, dissociated edge dislocations with two partial cores connected via a short stacking fault are found [82].

Completing this STEM characterization, shown in Fig. 6 are atomic-resolution cross-sectional HAADF images in the vicinity of the substrate/film interface (horizontal dashed lines) on LAO, STO, GSO, and PSO. Aside from the apparently sharp interfaces, particularly important is the observation of clear MDs, as marked by the symbols. Consistent with simple expectations and our prior papers [46,60], these interfacial MDs predominantly have in-plane Burgers vectors (yellow symbols), although on LAO some additional edge dislocations with out-of-plane Burgers vectors are found (red symbols). The latter have been connected to the anomalously broad RCs that can occur on substrates such as LAO, i.e., at very high lattice mismatch [60]. Of higher relevance to this paper is the clear evolution in MD density with lattice mismatch from PSO to LAO substrates (bottom to top in Fig. 6). This is quantified in Table I, where the top two rows give the expected average MD spacing calculated simply from the lattice mismatch and the measured average spacing from the images in Fig. 6. The agreement between expected and

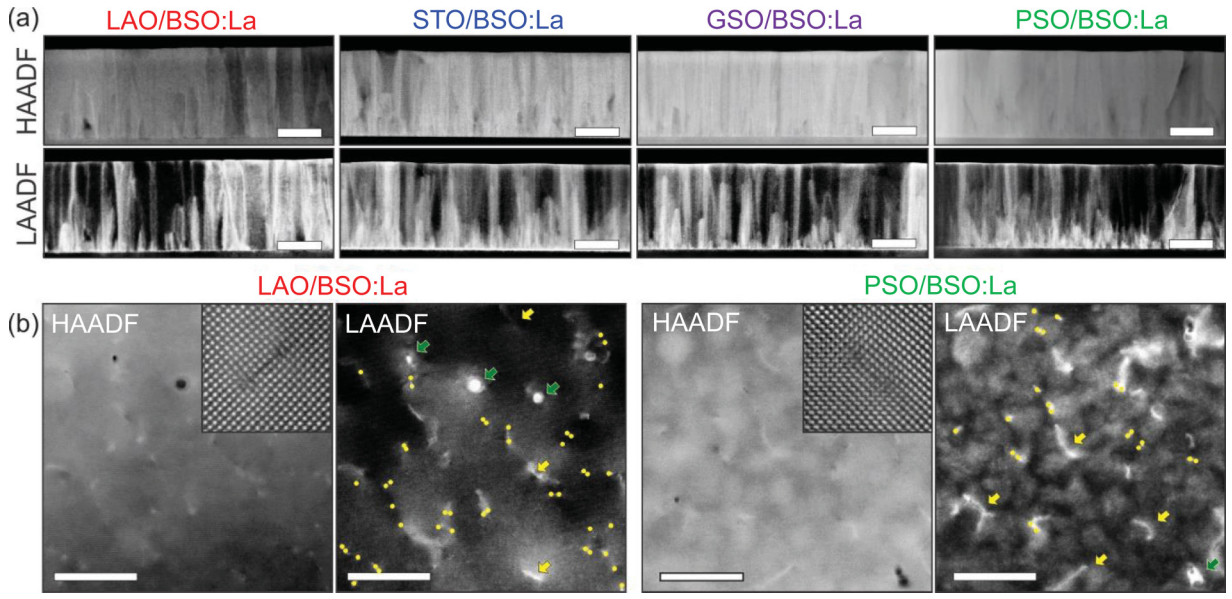

FIG. 5. Annular dark-field (ADF) scanning transmission electron microscopy (STEM) images of 200 nm thick $La_{0.02}Ba_{0.98}SnO_3$ (BSO:La) films grown at 1.9 Torr oxygen pressure, 900 °C deposition temperature and ∼1 nm min^{-1} deposition rate on $LaAlO_3$ (LAO), $SrTiO_3$ (STO), $GdScO_3$ (GSO), and $PrScO_3$ (PSO) substrates. (a) Cross-sectional high-angle ADF (HAADF; top) and low-angle ADF (LAADF) STEM images (bottom); scale bars are 100 nm. (b) Plan-view HAADF (left) and LAADF-STEM (right) images of the same films grown on LAO and PSO substrates; scale bars are 50 nm. In the LAADF images, yellow dots mark threading dislocations (TDs) of edge character, yellow arrows mark bright, high-strained regions (screw dislocations or grain boundary regions), and green arrows mark the partial voids discussed in the text. The insets show magnified regions around pairs of dissociated TDs (of edge character) connected via a short stacking fault.

measured average MD spacing is good on all substrates, the only caveat being the high relative uncertainty on PSO due to the high MD spacing. The subsequent rows in Table I show conversions of these average MD spacings (which vary from 11.3 ± 0.6 unit cells on LAO to 48.5 ± 14.5 unit cells on PSO) to MD densities, for which experimental values vary from $47 \pm 5 \times 10^{11}$ cm^{-2} on LAO to $3.1 \pm 1.8 \times 10^{11}$ cm^{-2} on PSO. Extracting the TD densities from plan-view STEM images of the type shown in Fig. 5(b) (on LAO and PSO) then enables comparison of the interfacial MD densities with the plan-view TD densities at this 200 nm thickness (Table I). Notably, the factor of 15 increase in MD density on LAO compared with PSO (from $3.1 \pm 1.8 \times 10^{11}$ cm^{-2} to $47 \pm 5 \times 10^{11}$ cm^{-2}) results in only a factor of two increase in TD density (from 0.87×10^{11} cm^{-2} to 1.8×10^{11} cm^{-2}). This is a significant observation, indicating that TD and MD densities are, to a large extent, decoupled in these BSO:La films. This provides a plausible explanation for the findings in Fig. 3(c), where μ(300 K) is only weakly dependent on substrate at high T_{dep}, i.e., only weakly dependent on lattice

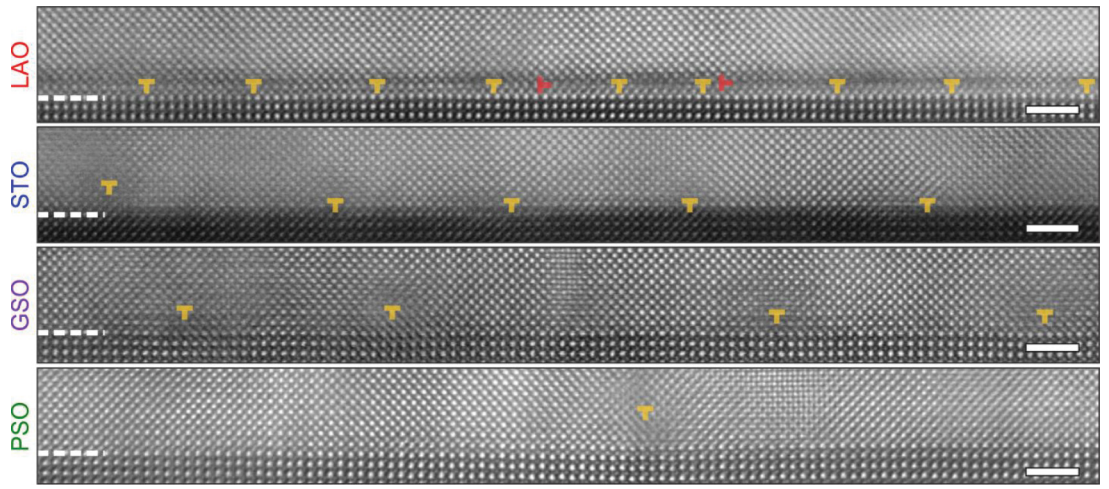

FIG. 6. Atomic-resolution cross-sectional high-angle annular dark-field (HAADF) scanning transmission electron microscopy (STEM) images of the substrate-film interfaces for the films shown in Fig. 5. These are 200 nm thick $La_{0.02}Ba_{0.98}SnO_3$ (BSO:La) films grown at 1.9 Torr oxygen pressure, 900 °C deposition temperature, and ∼1 nm min^{-1} deposition rate on $LaAlO_3$ (LAO), $SrTiO_3$ (STO), $GdScO_3$ (GSO), and $PrScO_3$ (PSO) substrates. Scale bars are 2 nm. Misfit dislocations (MDs) with in-plane and out-of-plane Burgers vector are marked yellow and red, respectively.

TABLE I. Average spacing [in units of $BaSnO_3$ (BSO) unit cells (u.c.$_{BSO}$)] and density (in units of 10^{11} cm^{-2}) of misfit dislocations (MDs) and threading dislocations (TDs) in 200 nm thick $La_{0.02}Ba_{0.98}SnO_3$ (BSO:La) films on $LaAlO_3$ (LAO), $SrTiO_3$ (STO), $GdScO_3$ (GSO), and $PrScO_3$ (PSO) substrates. These films were grown at 1.9 Torr oxygen pressure, 900 °C, and ∼1 nm min^{-1}, as in Figs. 5 and 6. Theoretical (theory) MD spacings and densities were calculated from the substrate lattice mismatch; experimental (expt.) MD and TD parameters were determined from cross-sectional and plan-view HAADF STEM images, respectively. Error bars represent 1 standard deviation.

	LAO/BSO:La	STO/BSO:La	GSO/BSO:La	PSO/BSO:La
MD spacing (theory; u.c.$_{BSO}$)	11.5	18.2	26.5	41.0
MD spacing (expt.; u.c.$_{BSO}$)	11.3 ± 0.6	19.4 ± 1.17	25.4 ± 2.6	48.5 ± 14.5
MD density (theory; 10^{11} cm^{-2})	44	17	8.5	3.5
MD density (expt.; 10^{11} cm^{-2})	47 ± 5.2	15.8 ± 1.8	9.3 ± 1.7	3.1 ± 1.8
TD density (expt.; 10^{11} cm^{-2})	1.8	–	–	0.87

mismatch; this is expected if the TDs that impact mobility have only weakly mismatch-dependent density. In terms of magnitudes, the $O(10^{11}\,\text{cm}^{-2})$ TD densities are in general agreement with the 10^{11}–$10^{12}\,\text{cm}^{-2}$ previously reported in BSO films [6,13,19,25–27,31,37,45,58].

Further evidence for the above conclusions is provided in Fig. 7, which summarizes the t dependence of the transport properties of sputtered BSO:La films, again at $T_{dep} = 900\,^{\circ}\text{C}$, $P_{O2} = 1.9$ Torr, and $R \approx 1$ nm min^{-1}. Figures 7(a)–7(c) plot the t dependence of the 300 K ρ, n, and μ, respectively, for films on LAO, STO, GSO, PSO, and MgO. Starting with n(300 K) in Fig. 7(b), at $t > 25$ nm, close correspondence is found with nominal La doping (horizontal dotted line), indicating essentially full dopant activation and negligible compensation, consistent with the $t = 80$ nm data in Fig. 3(b). At lower t, however, n(300 K) rapidly decreases by as much as an order of magnitude. This is ascribed to two effects: a substantially increased density of compensating defects at low t [in the interfacial MD-rich region (see Fig. 6)] as well as potential surface and/or interface depletion related to Fermi level pinning [12]. Moving to mobility [Fig. 7(c)], μ(300 K) also generally increases with t, but with distinctly different form to n(300 K). The increase with t is more gradual, consistent with the trends in TD density deduced from Fig. 4(i), where the mosaic spread gradually dampens with increasing t. The mobility is also only weakly dependent on substrate [as in Fig. 3(c) at high T_{dep}], again consistent with TD densities that depend only weakly on mismatch. In terms of magnitude, μ(300 K) reaches ∼60−80 cm^2 V^{-1} s^{-1} at 200 nm and above, where a weak, but nevertheless clear, trend with substrate emerges. Specifically, symmetry-mismatched MgO substrates result in the lowest mobility, while on symmetry-matched perovskite substrates μ(300 K) increases slightly with increasing lattice mismatch. This can be seen at $t \approx 200$ nm in Fig. 7(c), but is better highlighted in Fig. 7(d). In this panel, quite counterintuitively, μ(300 K) increases monotonically from 69 cm^2 V^{-1} s^{-1} on PSO (−2.2% mismatch) to 81 cm^2 V^{-1} s^{-1} on SLAO (−9.6%). Given that the TD density depends only weakly on mismatch and considering Fig. 4(g), for example, we infer that the trend in Fig. 7(d) may reflect the decreasing critical thickness for strain relaxation with increasing mismatch, which results in larger fractions of the 200 nm thickness being strain relaxed. The mobility thus appears to be improved in the relaxed portion of such films, a phenomenon that would benefit from further research, particularly as a function of doping. Figure 7(a) finally plots the t dependence of ρ(300 K), which due to the trends in Figs. 7(b) and 7(c) exhibits a rapid decrease up to ∼25 nm before gradually decreasing to the highest t studied.

Figure 8 provides further information via the T dependence of ρ, n, and μ at representative t of 11, 29, 35, 74, 93, and 118 nm, using STO substrates as an example. Despite the significant compensation at low t, even the 11 nm film in Fig. 8(b) presents degenerate doping. As shown in Fig. 8(c), such thin films also exhibit rather T-independent μ, decreasing only weakly on cooling. As t is increased, $\mu(T)$ then gradually evolves into a clearly phonon-limited form, the 61 cm^2 V^{-1} s^{-1} mobility at 300 K increasing to 91 cm^2 V^{-1} s^{-1} at low T in 118 nm thick films. The resulting $\rho(T)$ [Fig. 8(a)] evolves from exhibiting a weak increase in the low T limit in the 11 nm film, to clear metallic behavior with positive $d\rho/dT$ at all T in the thickest films. Again, weak localization is responsible for the low T upturn in the thinner films [79].

D. Influence of deposition rate

Based on the findings from Secs. III B and III C, the growth conditions were next fixed at $T_{dep} = 900\,^{\circ}\text{C}$ and $P_{O2} = 1.9$ Torr, the film thickness was held constant at an intermediate value (∼35 nm), and the deposition rate R was systematically varied. This was achieved by varying the dc sputter power, primarily through current control. Figure 9 summarizes the impacts on structure and microstructure (left panels) and transport (right panels), plotting (a) a_{op}, (b) Λ/t, (c) RC FWHM, (d) ρ(300 K), (e) n(300 K), and (f) μ(300 K). Aside from the previously discussed trends in a_{op} with substrate at this t (which are consistent with Fig. 4(g) at $R \approx 1$ nm min^{-1}, $t \approx 35$ nm), the striking feature in Fig. 9(a) is the clear lattice expansion below 0.25 nm min^{-1}, which occurs across all substrates. As seen in Figs. 9(b) and 9(c), although sample-to-sample variations arise, this is accompanied by a clear decrease in Λ/t (i.e., a decrease in through-thickness structural coherence) and a small increase in RC FWHM (i.e., an increase in mosaic spread). Importantly, at these low rates, which correspond to dc powers <30 W, the plasma plume in the deposition system becomes faint, with tendencies to inhomogeneity across the surface of the target as well as current and voltage fluctuations. We thus believe that the behavior at $R < 0.25$ nm min^{-1} in Figs. 9(a)–9(c) is likely due to spatial variations in structure and composition, resulting in specular WAXRD and RC peak broadening, and lattice parameter expansion, the latter reflecting local nonstoichiometric regions.

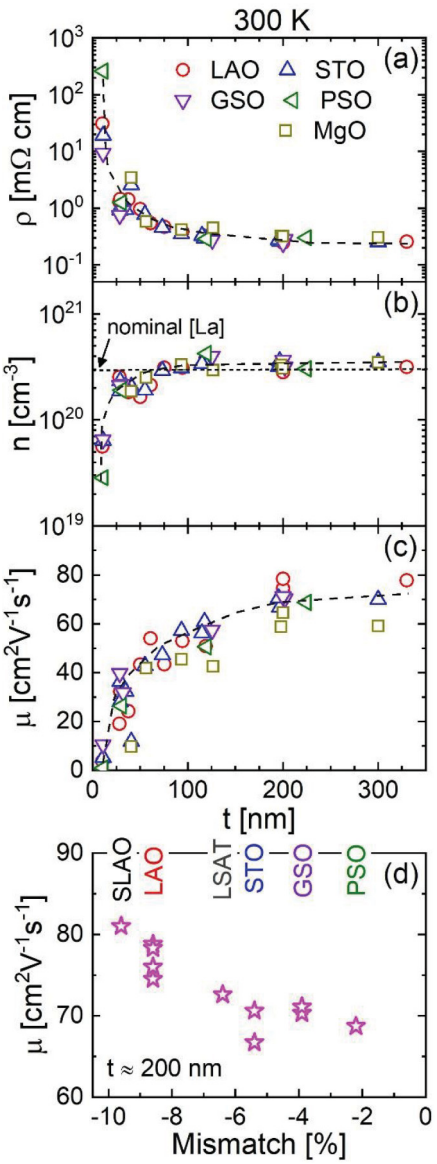

FIG. 7. Thickness (t) dependence of the 300 K (a) resistivity (ρ), (b) Hall electron density (n), and (c) Hall mobility (μ) for $La_{0.02}Ba_{0.98}SnO_3$ (BSO:La) films on MgO, $LaAlO_3$ (LAO), $SrTiO_3$ (STO), $GdScO_3$ (GSO), and $PrScO_3$ (PSO) substrates. Oxygen pressure, deposition temperature, and rate were held constant at 1.9 Torr, 900 °C, and ∼1 nm min^{-1}, respectively. The horizontal black dotted line in (b) marks the nominal n for full dopant activation. Other black dashed lines are guides to the eye. (d) Lattice mismatch dependence of the 300 K mobility under the same growth conditions for 200 nm thick films. The relevant substrates (all perovskites) are marked.

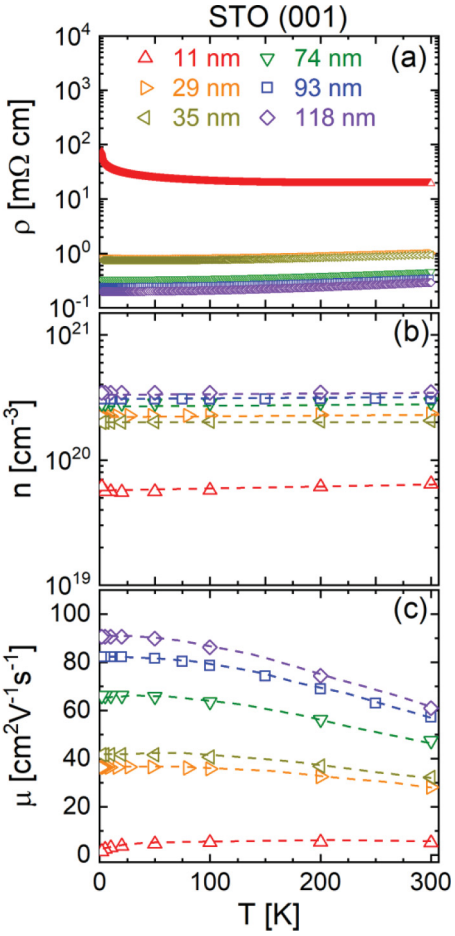

FIG. 8. Temperature (T) dependence of (a) resistivity (ρ), (b) Hall electron density (n), and (c) Hall mobility (μ), for $La_{0.02}Ba_{0.98}SnO_3$ (BSO:La) films of various thickness (t) on representative $SrTiO_3$ (STO) substrates. Oxygen pressure, deposition temperature, and rate were held constant at 1.9 Torr, 900 °C, and ∼1 nm min^{-1}, respectively. Colored dashed lines are guides to the eye.

As would be expected, Figs. 9(e) and 9(f) then reveal distinct decreases in n(300 K) and μ(300 K) below ∼0.25 nm min^{-1} (factors of 2–3 in each case), resulting in a significant increase in ρ(300 K). [Note that the arrows in Figs. 9(d)–9(f) indicate that further reducing R leads to much larger ρ, and much lower n and μ, off scale in those panels.] The increase in ρ(300 K) is accompanied by the onset of nonnegligible resistance anisotropy in van der Pauw measurements, which was not detected under other conditions in this paper, further supporting the conclusion of spatial inhomogeneity in structure and composition. The only other noteworthy feature in Figs. 9(e) and 9(f) is the rise in n(300 K), and particularly μ(300 K), with decreasing R, before the conspicuous drop below 0.25 nm min^{-1}. An apparently optimal rate thus emerges at around 0.25 nm min^{-1}. It must be emphasized, however, that this optimization of μ(300 K) by decreasing R (at this ∼35 nm thickness) is not preserved at higher t. As shown in Fig. S3 in the Supplemental Material [80], at $R = 0.25$ nm min^{-1}, μ(300 K) simply increases faster with increasing t [compared with the 1 nm min^{-1} case in Fig. 7(c)], enabling attainment of good μ(300 K) at lower t (<50 nm) but with no increase in the maximum attainable μ(300 K). The peak in μ(300 K) vs R in Fig. 9(f) is thus of limited utility, outside of optimization of mobility at low t. This is particularly so given the onset of plasma instability, structural and chemical inhomogeneity, and transport anisotropy at just marginally lower R, not to mention the convenience and improved throughput of higher R. Nevertheless, the ability to improve mobility at low t by decreasing R provides another suggestion [along with the nonsaturation of μ(300 K) vs T_{dep} in Fig. 3(c)] that thermal annealing could be beneficial. This is tackled next.

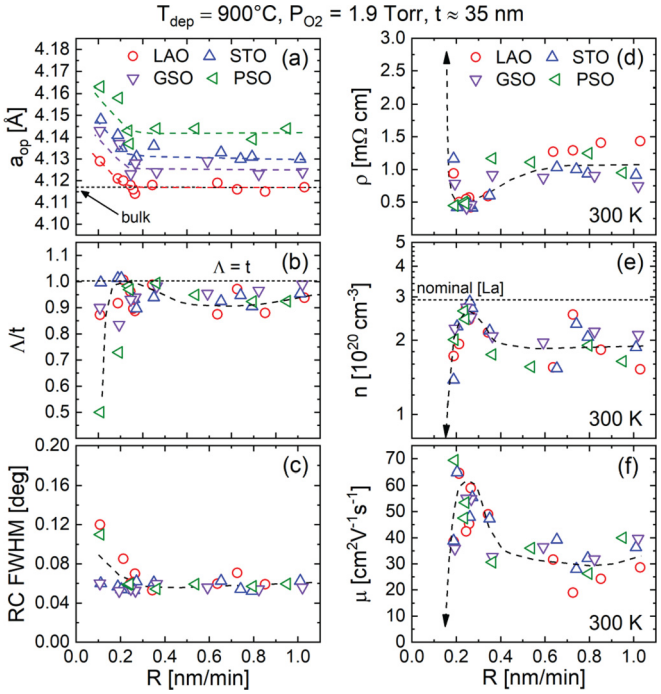

FIG. 9. Deposition rate (R) dependence of (a) the out-of-plane lattice parameter (a_{op}), (b) the Scherrer length-to-thickness ratio (Λ/t), (c) the 002 rocking curve full width at half maximum (RC FWHM), (d) the 300 K resistivity (ρ), (e) the 300 K Hall electron density (n), and (f) the 300 K Hall mobility (μ) for $La_{0.02}Ba_{0.98}SnO_3$ (BSO:La) films on $LaAlO_3$ (LAO), $SrTiO_3$ (STO), $GdScO_3$ (GSO), and $PrScO_3$ (PSO) substrates. The deposition temperature (T_{dep}), oxygen pressure (P_{O2}), and thickness (t) were held constant at 900 °C, 1.9 Torr, and ∼35 nm, respectively. The horizontal black dashed lines in (a), (b), and (e) mark the bulk lattice parameter $\Lambda = t$ and the nominal n for full dopant activation, respectively. Colored dashed lines are guides to the eye. The arrows in the right panels indicate that lower R values resulted in much larger ρ, lower n, and lower μ, off scale in (d) and (e).

E. Postdeposition annealing

Based on the above and given the recent literature successes with improvement of mobility in doped BSO films by thermal treatment, particularly under reducing conditions [21,23,24], postdeposition vacuum annealing was also studied. As discussed in Sec. II, this was done at $\sim 6 \times 10^{-7}$ Torr, at annealing temperatures (T_{anneal}) between 500 and 800 °C. In initial work, T_{dep}, P_{O2}, and R were fixed at 900 °C, 1.9 Torr, and 1 nm min^{-1}, respectively, and $t \approx 58$ nm films on MgO were studied, annealing for 1 h. MgO was selected for several reasons, including avoidance of parasitic conductivity due to V_O formation in the substrate (as would be likely in STO, for example [83]), and given the results in Secs. III A–III D, the greater potential for significant annealing-induced gains in structural quality. Shown in Figs. 10(a) and 10(b) are example specular WAXRD and RC scans taken on a BSO:La film before and after annealing at 750 °C. As shown in Fig. 10(a), single-phase character is retained after annealing (confirmed by wider-range 2θ scans), the main annealing-induced changes being a downshift in peak position and some peak narrowing, indicating expansion of a_{op} and an increase in Λ. As shown in Fig. 10(b), these changes are accompanied by a substantial decrease in RC FWHM (0.92 to 0.52 °), indicating improved mosaicity with annealing.

Given these promising initial findings, a systematic study was performed as a function of T_{anneal}, leading to the structural and microstructural results in Figs. 10(c)–10(f). This was done in a mode where six nominally identical BSO:La films were grown, then individually subjected to 1 h vacuum anneals at 500–800 °C. As indicated by the dotted black lines in Figs. 10(c) and 10(d), the average as-grown a_{op} and RC FWHM were 4.116 Å and 0.88 °, respectively, for these ∼58 nm films on MgO [consistent with Figs. 4(g) and 4(i)]. Apparent in the figures are a significant monotonic increase in a_{op} (up to 4.120 Å at 750 °C) before an abrupt flattening, along with a similarly significant decrease in the RC FWHM (reaching almost a factor of two) before a sharp increase at $T_{anneal} = 800$ °C. As shown on the right axis of Fig. 10(f), Λ/t correspondingly increases with T_{anneal} up to 750 °C (by up to 28%), before falling precipitously at 800 °C. The abrupt structural degradation at >750 °C is clarified in Figs. 10(g)–10(i), where the RMS surface roughness from AFM is seen to increase moderately from 0.5 to 1.9 nm after annealing at 750 °C but then drastically to ∼25 nm after annealing at 800 °C. Extreme roughening, pitting, and even recrystallization (potentially associated with a second phase) [24,29] can be seen in Fig. 10(i), placing an upper limit on T_{anneal} of 750 °C under these growth conditions. Figures 10(e) and 10(f) then show the accompanying annealing-induced changes in 300 K n and μ. Note that the as-grown films here had average $n(300\,\text{K}) = 2.1 \times 10^{20}$ cm^{-3} and average $\mu(300\,\text{K}) = 33$ cm^2 V^{-1} s^{-1}. In Fig. 10(e), the annealing-induced change in 300 K Hall electron density (Δn) is seen to grow to $\sim 5 \times 10^{19}$ cm^{-3} with increasing T_{anneal}, plateau in this range, and then drop to a negative value (i.e., an annealing-induced decrease) at 800 °C. Correspondingly, the annealing-induced change in 300 K mobility ($\Delta\mu$) in Fig. 10(f) is seen to increase to 66–72% at $T_{anneal} = 600-750$ °C before rapidly dropping to a negative value at 800 °C.

These results indicate significant improvements in structural coherence [Fig. 10(f)] and mosaic spread [Fig. 10(d)] for T_{anneal} up to 750 °C, which induce up to 72% increases in μ(300 K) [Fig. 10(f)], reaching 60 cm^2 V^{-1} s^{-1} in these 58 nm thick films on MgO. This is followed by an abrupt decrease in structural quality and smoothness for $T_{anneal} >$ 750 °C, with a concomitant mobility drop. Critical to our interpretation of the annealing-induced mobility enhancement for $T_{anneal} \leqslant 750$ °C is the expansion in a_{op} by as much as 0.004 Å [Fig. 10(c)] and the accompanying $\Delta n \approx 5 \times 10^{19}$ cm^{-3} [Fig. 10(e)]. Both of these observations are consistent with V_O formation, the expanded a_{op} agreeing with our prior paper on vacuum annealing of undoped BSO films [46], and the Δn being quantitatively consistent with our prior observations in vacuum-annealed BSO films [12,46] and bulk crystals [15]. The latter papers [12,15,46] provided strong evidence of V_O-induced n-type doping in BSO, which has been suggested to play a role in vacuum annealing-induced mobility enhancement in La-doped BSO also [21,23]. In the current case, while the annealing-induced increase in n ($\sim 5 \times 10^{19}$ cm^{-3}, from an initial 2.1×10^{20} cm^{-3}) may play some direct role in mobility improvement (via improved screening of charged defects), it

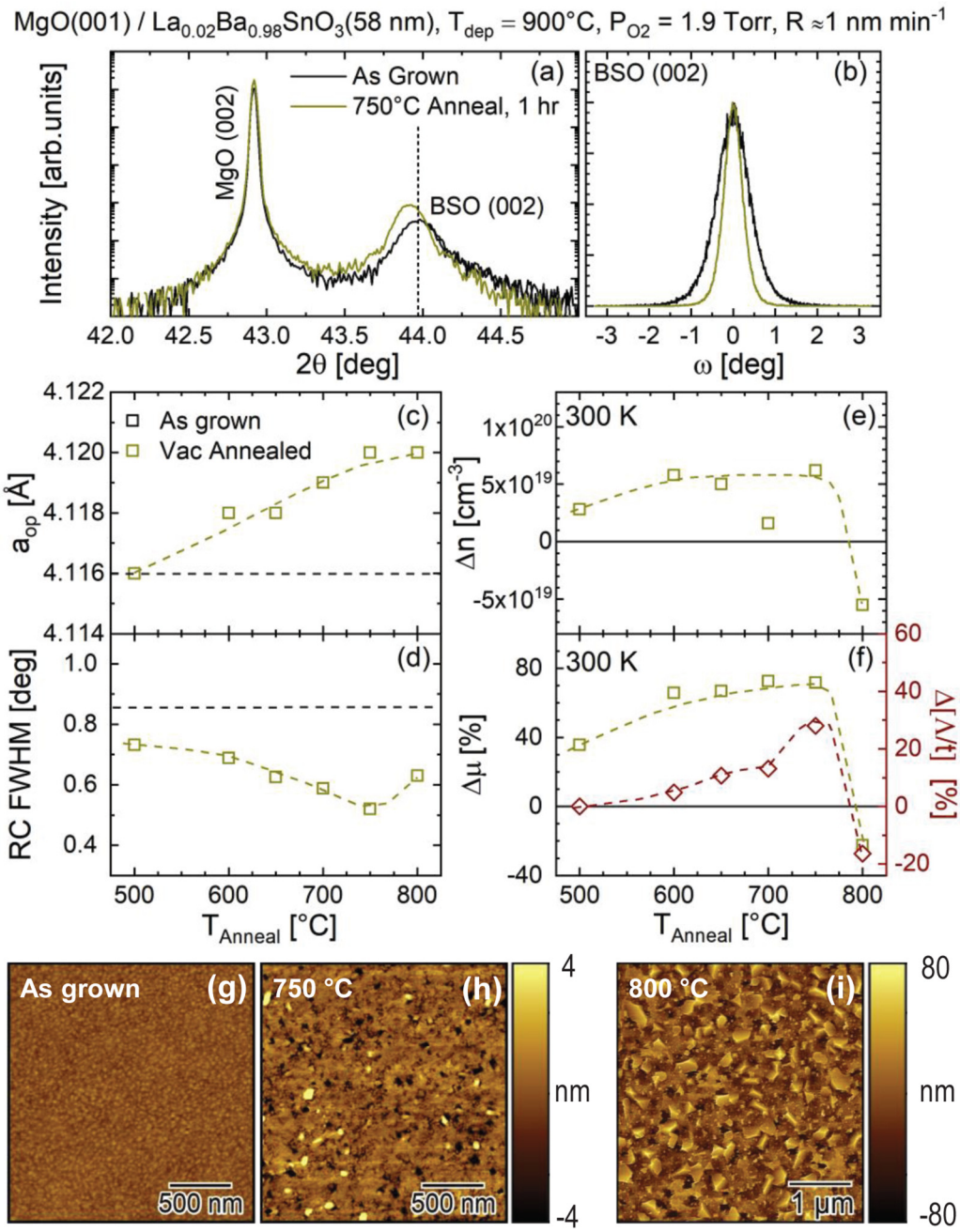

FIG. 10. (a) High-resolution wide-angle specular x-ray diffraction around the 002 film and substrate reflections and (b) corresponding 002 film rocking curves from a $La_{0.02}Ba_{0.98}SnO_3$ (BSO:La) film before and after vacuum annealing for 1 h at 750 °C. The vertical black dashed line in (a) corresponds to the bulk lattice parameter. All data in this figure are from films deposited on MgO at 900 °C, in 1.9 Torr of O_2, at ∼1 nm min^{-1}, to ∼58 nm thickness. (c)–(f) Annealing temperature (T_{anneal}) dependence of (c) the out-of-plane lattice parameter (a_{op}), (d) the 002 film rocking curve full width at half maximum (RC FWHM), (e) the annealing-induced change in 300 K Hall electron density (Δn), and (f) the annealing-induced change in 300 K Hall mobility ($\Delta\mu$). Shown on the right axis in (f) is the annealing-induced change in Scherrer length-to-thickness ratio ($\Delta[\Lambda/t]$). The horizontal black dashed lines in (c) and (d) represent average values for as-grown films; all other dashed lines are guides to the eye. Contact-mode atomic force microscopy (AFM) images of (g) an as-grown film, (h) a 750 °C annealed film, and (i) an 800 °C annealed film; scale bars are provided.

is likely that microstructural improvements (potentially facilitated by V_O formation [21,23]) play the major role. In addition to the improvement in mosaicity [Fig. 10(d)] and out-of-plane structural coherence [Fig. 10(f)], Fig. S4 in the Supplemental Material [80] further reveals an annealing-induced increase in in-plane grain size. This is deduced from an asymmetric RSM about the 103 reflection of a MgO/BSO:La(200 nm) film, suggesting doubling of the in-plane coherence length from 13 to 26 nm after a 1 h 750 °C anneal. Consistent with some prior papers [21,23], we thus consider microstructural improvements to play the major role in the observed vacuum annealing-induced mobility enhancement.

Based on the results in Fig. 10, several additional annealing experiments were performed. These explored the

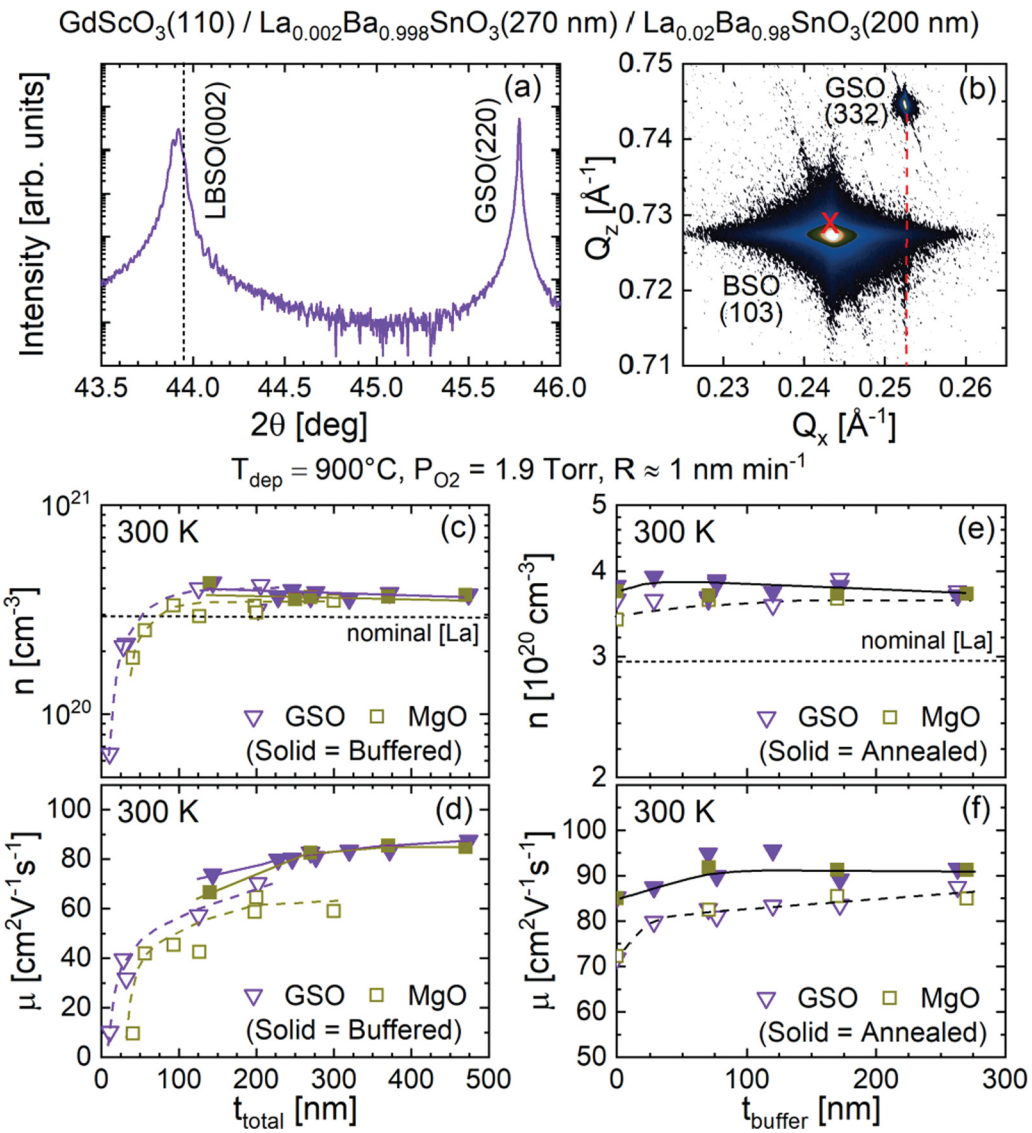

FIG. 11. (a) High-resolution wide-angle specular x-ray diffraction around the 002 film and 220 substrate reflections and (b) 103 reciprocal space map from a representative $GdScO_3/La_{0.002}Ba_{0.998}SnO_3$ (270 nm)/$La_{0.02}Ba_{0.98}SnO_3$(200 nm) heterostructure after vacuum annealing at 650 °C for 15 min. The vertical black dashed line in (a) and the red X in (b) correspond to the bulk BSO:La lattice parameter. (c) and (d) 300 K Hall electron density (n) and mobility (μ) vs total film thickness ($t_{total} = t_{buffer} + t_{active}$) for films on MgO and $GdScO_3$ (GSO) substrates. Open points represent unbuffered films [as in Figs. 7(b) and 7(c)] and solid points buffered films (t_{buffer} = 100–270 nm). (e) and (f) 300 K n and μ vs t_{buffer} for constant t_{active} = 200 nm, again for films on MgO and GSO. Open and solid points represent as-grown and 650 °C, 15 min, vacuum-annealed films, respectively. All films in the figure were deposited at 900 °C in 1.9 Torr of O_2 at ∼1 nm min^{-1}. The horizontal black dashed lines in (c) and (e) mark the nominal n for full dopant activation; all other dashed and solid lines are guides to the eye.

annealing temperature, time, and pressure, in some cases performing consecutive anneals on individual films. These strategies were somewhat effective under certain conditions: an LAO/BSO:La(59 nm) film, for example, exhibited $\mu(300\,K) = 54\,cm^2\,V^{-1}\,s^{-1}$ as deposited, then $70\,cm^2\,V^{-1}\,s^{-1}$ after a 1 h vacuum anneal at 650 °C at $O(10^{-7}$ Torr), and $76\,cm^2\,V^{-1}\,s^{-1}$ after an additional 4 h of 650 °C vacuum annealing at $O(10^{-4}$ Torr). Generally, a tradeoff was found with respect to microstructural improvement vs surface degradation at high annealing temperatures and times [24,29], dependent on conditions such as pressure. Further work exploring and refining this process would be worthwhile. In the final set of investigations in this paper, however, which explores the impacts of buffer layer incorporation in tandem with postdeposition thermal treatment, the annealing conditions were simply fixed at a conservative 650 °C and 15 min to avoid surface degradation. GSO substrates were also explored in these studies, extending the results of Fig. 10 beyond MgO.

F. Buffer layer incorporation

Summarized in Fig. 11 are the effects of adding insulating BSO buffer layers between the substrate and BSO:La films. Based on Secs. III B–III E, this was explored in films grown at T_{dep} = 900 °C, P_{O2} = 1.9 Torr, and $R \approx 1$ nm min^{-1}, comparing GSO with MgO substrates and as-grown with

vacuum-annealed (650 °C, 15 min) cases. Due to the higher deposition rates for dc compared to rf sputtering and the desire to explore high thicknesses, the "insulating" BSO buffer layers were in fact grown from a lightly doped $Ba_{0.998}La_{0.002}SnO_3$ (i.e., $x = 0.002$) target. As shown in Supplemental Material Fig. S5 [80], this 0.2% La doping results in at most $n \approx 2 \times 10^{19}$ cm^{-3} (at high t) compared with typically 3×10^{20} cm^{-3} in 2%-La-doped films. Given that the mobilities in such lightly doped layers were found to be similar or lower than in heavier-doped films, the resistivity (and thus sheet resistance) is substantially larger at the same t, resulting in only modest current shunting through buffer layers in buffered films (typically <5%). This shunting effect was nevertheless accounted for via a simple two-channel conduction model [14], as described in the caption to Fig. S5; typical impacts on extracted μ(300 K) values were <2%.

Shown in Figs. 11(a) and 11(b) are WAXRD and RSM scans from an example annealed GSO/BSO($x = 0.002$, $t =$ 270 nm)/BSO($x = 0.02$, $t = 200$ nm) heterostructure. An intense 002 peak from the combined buffer and active layers is found close to the expected position for bulk BSO [dotted black line in Fig. 11(a)], the 103 peak in the RSM [Fig. 11(b)] occurring near the fully relaxed position (red cross). Consistent with Fig. 4(g), such thick films are thus essentially strain relaxed. The impact of buffer layer incorporation on the 300 K transport properties of the active (i.e., heavily doped) layer is then displayed in Figs. 11(c)–11(f), showing n (top panels) and μ (bottom panels). In Figs. 11(c) and 11(d), the data are shown vs $t_{\text{total}} = t_{\text{buffer}} + t_{\text{active}}$, for thick buffer layers ($t_{\text{buffer}} =$ 100–270 nm) and variable thickness active layers ($t_{\text{active}} =$ 30–200 nm). Unbuffered films are also shown for comparison in Figs. 11(c) and 11(d), the solid and open points corresponding to buffered and unbuffered films, respectively. [The open points thus correspond to Figs. 7(b) and 7(c).] The obvious features are the consistent n(300 K) vs t_{total} curves in buffered and unbuffered films [Fig. 11(c)] and, most importantly, the significant boost to μ(300 K) [Fig. 11(d)] in buffered films. The buffered curve in Fig. 11(d) in fact lies entirely above the unbuffered data in the overlap region, μ(300 K) in the buffered case rising gradually with t_{total}, reaching 87 and 85 cm^2 V^{-1} s^{-1} at $t_{\text{total}} \approx 470$ nm on GSO and MgO, respectively. This effect of buffer layer incorporation is displayed in a complementary fashion in Figs. 11(e) and 11(f), where t_{active} is fixed at 200 nm, and t_{buffer} is varied from 0 to 270 nm. The data here are additionally shown for both as-grown (open points) and annealed (650 °C, 15 min) cases. Before annealing, the effect of buffer layer incorporation is evident mostly in the gradual increase in μ(300 K) with increasing t_{buffer}, reaching 85−87 cm^2 V^{-1} s^{-1} [consistent with Fig. 11(d)]. Annealing then induces further mobility enhancement on both substrates, resulting in μ(300 K) > 90 cm^2 V^{-1} s^{-1}, including 96 cm^2 V^{-1} s^{-1} on GSO at $t_{\text{buffer}} = 120$ nm, $t_{\text{active}} = 200$ nm. Buffer layer incorporation and vacuum annealing thus both induce nontrivial mobility enhancements, the combination of both resulting in the highest μ(300 K) in this paper. We ascribe the annealing-induced enhancement primarily to microstructural improvements (such as increased in-plane grain size and through-thickness structural coherence and decreased mosaicity, as discussed in Sec. III E). The buffer-layer induced mobility enhancement, on the other hand, is ascribed to a decrease of the TD density [6,13,26,27,31,37–39], consistent with the conclusions from Figs. 4(i) and 7(c), as well as the ∼0.01 ° RC FWHM for the film shown in Figs. 11(a) and 11(b), for example. The latter value can be compared with Fig. 4(i), confirming a significant decrease in mosaic spread in buffered and annealed films. The $\Lambda/t = 0.75$ in this film is similarly impressive.

IV. CONCLUSIONS AND SUMMARY

With respect to the central issue of room temperature mobility optimization, as noted above, Fig. 11(f) reveals maximum μ(300 K) of 96 cm^2 V^{-1} s^{-1} in vacuum-annealed GSO/BSO($x = 0.002$, $t = 120$ nm)/BSO($x = 0.02$, $t = 200$ nm) films, and 92 cm^2 V^{-1} s^{-1} in MgO/BSO($x =$ 0.002, $t = 70$ nm)/BSO($x = 0.02$, $t = 200$ nm). Further highlighting the transport properties of such optimized films, Fig. S6 in the Supplemental Material [80] shows the T-dependent ρ, n, and μ of an annealed GSO/BSO($x = 0.002$, $t =$ 120 nm)/BSO($x = 0.02$, $t = 200$ nm) heterostructure grown at 900 °C, 1.9 Torr, and 1 nm min^{-1}. The 96 cm^2 V^{-1} s^{-1} room temperature mobility rises to 165 cm^2 V^{-1} s^{-1} as $T \to 0$, the residual resistivity and residual resistivity ratio reaching 104 $\mu\Omega$cm and 1.63, respectively. Employing a simple Drude model and a free-electronlike density of states (with weakly n-dependent m_e^* [28]), these values translate to an elastic scattering time of ∼11 fs and a mean-free path of ∼14 nm, at a Fermi energy of ∼630 meV.

It is important to emphasize that, while these champion sputtered film mobilities involve both buffer layers and thermal annealing, μ(300 K) of up to 87 cm^2 V^{-1} s^{-1} can be achieved without postdeposition thermal treatment. This can be seen from Figs. 11(d) and 11(f), where 87 cm^2 V^{-1} s^{-1} is attained in a GSO/BSO($x = 0.002$, $t = 270$ nm)/BSO($x =$ 0.02, $t = 200$ nm) film, the equivalent value on MgO being only marginally smaller at 85 cm^2 V^{-1} s^{-1}. Without the use of buffer layers, the peak μ(300 K) in this paper was 92 cm^2 V^{-1} s^{-1}, achieved in vacuum-annealed LAO/BSO($x =$ 0.02, $t = 200$ nm) films. We contend that these optimized mobility values are significant in at least three ways. First, they represent substantial improvement over prior sputtered BSO, where the highest μ(300 K) reported (without electrolyte gating) seems to have been 30 cm^2 V^{-1} s^{-1} [12,14,34,35,46,58,59]. Second, these results place sputtered BSO:La films at a level of electronic quality comparable with the far more extensively studied PLD-grown material [1,2,8,17–33,39], which is significant given the scalability, throughput, and industrial relevance of sputter deposition. Thirdly, it seems highly likely that further work could improve upon these results, taking sputtered BSO beyond 100 cm^2 V^{-1} s^{-1} room temperature mobility. At heavy doping, where the highest quality BSO films are thought to have mobility limited by ionized impurity scattering [1,2,5,13,26–28,52,63], one probable cause of lower μ in sputtered films is higher densities of charged point defects. Two obvious routes to improvement in this regard are further attention to precise stoichiometry control and purity improvement. The weak link regarding the latter is likely the purity of the ceramic sputtering targets, which could be improved by further refinement of

synthesis conditions and through improved starting material purity, particularly the only 99.9% pure SnO_2 (Sec. II).

In summary, we have presented an exhaustive study of the interrelationships between deposition parameters, structure and microstructure, and electronic transport properties in epitaxial BSO:La films grown by high-pressure-oxygen reactive sputtering. The latter is a scalable, high-throughput deposition technique in the industry-standard sputtering family. Target synthesis conditions, substrate choice, deposition temperature, film thickness, deposition rate, postdeposition vacuum annealing conditions, and buffer layer incorporation have all been investigated, providing detailed information on trends in structural and microstructural parameters and their interplay with electronic transport (particularly defect densities and measures of microstructural quality). The room temperature electron mobility was thus optimized to 96 $cm^2\,V^{-1}\,s^{-1}$ in annealed GSO/BSO(120 nm)/BSO:La(200 nm) heterostructures, 92 $cm^2\,V^{-1}\,s^{-1}$ in unbuffered films, and 87 $cm^2\,V^{-1}\,s^{-1}$ in as-grown films (without postdeposition annealing). In addition to providing valuable understanding of synthesis-structure-property relationships in thin film BSO:La via a complementary growth method to PLD and MBE, these results establish sputtered mobilities competitive with PLD-grown material. We suggest that room temperature mobilities in excess of 100 $cm^2\,V^{-1}\,s^{-1}$ are very likely possible with further refinements of BSO sputter deposition.

ACKNOWLEDGMENTS

This paper was supported primarily by the US Department of Energy through the University of Minnesota (UMN) Center for Quantum Materials under DE-SC-0016371. Electron microscopy work by H.Y., J.S.J., and K.A.M was supported by the National Science Foundation (NSF) through the UMN Materials Research Science and Engineering Center (MRSEC) under DMR-1420013 and DMR-2011401. H.Y. also acknowledges a fellowship from the Samsung Scholarship Foundation, Republic of Korea. Parts of this paper were performed in the Characterization Facility, UMN, which receives partial support from NSF through the MRSEC program.

[1] H. J. Kim, U. Kim, H. M. Kim, T. H. Kim, H. S. Mun, B.-G. Jeon, K. T. Hong, W.-J. Lee, C. Ju, K. H. Kim, and K. Char, Appl. Phys. Express **5**, 061102 (2012).

[2] H. J. Kim, U. Kim, T. H. Kim, J. Kim, H. M. Kim, B.-G. Jeon, W.-J. Lee, H. S. Mun, K. T. Hong, J. Yu, K. Char, and K. H. Kim, Phys. Rev. B **86**, 165205 (2012).

[3] X. Luo, Y. S. Oh, A. Sirenko, P. Gao, T. A. Tyson, K. Char, and S.-W. Cheong, Appl. Phys. Lett. **100**, 172112 (2012).

[4] S. Ismail-Beigi, F. J. Walker, S. W. Cheong, K. M. Rabe, and C. H. Ahn, APL Mater. **3**, 062510 (2015).

[5] J. H. Lee, H. J. Kim, J. Kang, D. H. Jang, T. H. Kim, J. H. Lee, and K. H. Kim, Annu. Rev. Mater. Res. **47**, 391 (2017).

[6] Z. Wang, H. Paik, Z. Chen, D. A. Muller, and D. G. Schlom, APL Mater. **7**, 022520 (2019).

[7] K. Krishnaswamy, L. Bjaalie, B. Himmetoglu, A. Janotti, L. Gordon, and C. G. Van De Walle, Appl. Phys. Lett. **108**, 083501 (2016).

[8] U. Kim, C. Park, T. Ha, Y. M. Kim, N. Kim, C. Ju, J. Park, J. Yu, J. H. Kim, and K. Char, APL Mater. **3**, 036101 (2015).

[9] J. Yue, A. Prakash, M. C. Robbins, S. J. Koester, and B. Jalan, ACS Appl. Mater. Interfaces **10**, 21061 (2018).

[10] S. S. Shin, E. J. Yeom, W. S. Yang, S. Hur, M. G. Kim, J. Im, J. Seo, J. H. Noh, and S. I. Seok, Science **356**, 167 (2017).

[11] S. Raghavan, T. Schumann, H. Kim, J. Y. Zhang, T. A. Cain, and S. Stemmer, APL Mater. **4**, 016106 (2016).

[12] K. Ganguly, A. Prakash, B. Jalan, and C. Leighton, APL Mater. **5**, 056102 (2017).

[13] A. Prakash, P. Xu, A. Faghaninia, S. Shukla, J. W. Ager III, C. S. Lo, and B. Jalan, Nat. Commun. **8**, 15167 (2017).

[14] H. Wang, J. Walter, K. Ganguly, B. Yu, G. Yu, Z. Zhang, H. Zhou, H. Fu, M. Greven, and C. Leighton, Phys. Rev. Materials **3**, 075001 (2019).

[15] E. McCalla, D. Phelan, M. J. Krogstad, B. Dabrowski, and C. Leighton, Phys. Rev. Materials **2**, 084601 (2018).

[16] Z. Galazka, R. Uecker, K. Irmscher, D. Klimm, R. Bertram, A. Kwasniewski, N. Nauman, R. Schewski, M. Pietsch, U. Juda, A. Fiedler, M. Albrecht, S. Ganschow, T. Markurt, C. Guguschev, and M. Bickermann, J. Phys.: Condens. Matter **29**, 075701 (2017).

[17] U. S. Alaan, P. Shafer, A. T. N'Diaye, E. Arenholz, and Y. Suzuki, Appl. Phys. Lett. **108**, 042106 (2016).

[18] U. S. Alaan, F. J. Wong, J. J. Ditto, A. W. Robertson, E. Lindgren, A. Prakash, G. Haugstad, P. Shafer, A. T. N'Diaye, D. Johnson, E. Arenholz, B. Jalan, N. D. Brwoning, and Y. Suzuki, Phys. Rev. Materials **3**, 124402 (2019).

[19] A. V. Sanchela, M. Wei, H. Zensyo, B. Feng, J. Lee, G. Kim, H. Jeen, Y. Ikuhara, and H. Ohta, Appl. Phys. Lett. **112**, 232102 (2018).

[20] A. V. Sanchela, M. Wei, J. Lee, G. Kim, H. Jeen, B. Feng, Y. Ikuhara, H. J. Cho, and H. Ohta, J. Mater. Chem. C **7**, 5797 (2019).

[21] H. J. Cho, T. Onozato, M. Wei, A. Sanchela, and H. Ohta, APL Mater. **7**, 022507 (2019).

[22] H. J. Cho, B. Feng, T. Onozato, M. Wei, A. V. Sanchela, Y. Ikuhara, and H. Ohta, Phys. Rev. Materials **3**, 094601 (2019).

[23] D. Yoon, S. Yu, and J. Son, NPG Asia Mater. **10**, 363 (2018).

[24] S. Yu, D. Yoon, and J. Son, Appl. Phys. Lett. **108**, 262101 (2016).

[25] H. Mun, U. Kim, H. M. Kim, C. Park, T. H. Kim, H. J. Kim, K. H. Kim, and K. Char, Appl. Phys. Lett. **102**, 252105 (2013).

[26] J. Shin, Y. M. Kim, Y. Kim, C. Park, and K. Char, Appl. Phys. Lett. **109**, 262102 (2016).

[27] J. Shiogai, K. Nishihara, K. Sato, and A. Tsukazaki, AIP Adv. **6**, 065305 (2016).

[28] C. A. Niedermeier, S. Rhode, K. Ide, H. Hiramatsu, H. Hosono, T. Kamiya, and M. A. Moram, Phys. Rev. B **95**, 161202(R) (2017).

[29] G. Anoop, E. Y. Park, S. Lee, and J. Y. Jo, Electron. Mater. Lett. **11**, 565 (2015).

[30] P. V. Wadekar, J. Alaria, M. O'Sullivan, N. L. O. Flack, T. D. Manning, L. J. Phillips, K. Durose, O. Lozano, S. Lucas, J. B.

Claridge, and M. J. Rosseinsky, Appl. Phys. Lett. **105**, 052104 (2014).
[31] A. P. Nono Tchiomo, W. Braun, B. P. Doyle, W. Sigle, P. van Aken, J. Mannhart, and P. Ngabonziza, APL Mater. **7**, 041119 (2019).
[32] S. Sallis, D. O. Scanlon, S. C. Chae, N. F. Quackenbush, D. A. Fischer, J. C. Woicik, J.-H. Guo, S. W. Cheong, and L. F. J. Piper, Appl. Phys. Lett. **103**, 042105 (2013).
[33] W.-J. Lee, H. J. Kim, E. Sohn, T. H. Kim, J.-Y. Park, W. Park, H. Jeong, T. Lee, J. H. Kim, K.-Y. Choi, and K. H. Kim, Appl. Phys. Lett. **108**, 082105 (2016).
[34] A. Tiwari and M.-S. Wong, Thin Solid Films **715**, 138427 (2020).
[35] B. C. Luo, X. S. Cao, K. X. Jin, and C. L. Chen, Curr. Appl. Phys. **16**, 20 (2016).
[36] Z. Lebens-Higgins, D. O. Scanlon, H. Paik, S. Sallis, Y. Nie, M. Uchida, N. F. Quackenbush, M. J. Wahila, G. E. Sterbinsky, D. A. Arena, J. C. Woicik, D. G. Schlom, and L. F. J. Piper, Phys. Rev. Lett. **116**, 027602 (2016).
[37] H. Paik, Z. Chen, E. Lochocki, A. Seidner H., A. Verma, N. Tanen, J. Park, M. Uchida, S. Shang, B. C. Zhou, M. Brützam, R. Uecker, Z. K. Liu, D. Jena, K. M. Shen, D. A. Muller, and D. G. Schlom, APL Mater. **5**, 116107 (2017).
[38] A. Prakash, P. Xu, X. Wu, G. Haugstad, X. Wang, and B. Jalan, J. Mater. Chem. C **5**, 5730 (2017).
[39] C. Park, U. Kim, C. J. Ju, J. S. Park, Y. M. Kim, and K. Char, Appl. Phys. Lett. **105**, 203503 (2014).
[40] R. J. Terry, N. Combs, C. D. McMillen, S. Stemmer, and J. W. Kolis, J. Cryst. Growth **536**, 125529 (2020).
[41] F.-Y. Fan, W.-Y. Zhao, T.-W. Chen, J.-M. Yan, J.-P. Ma, L. Guo, G.-Y. Gao, F.-F. Wang, and R.-K. Zheng, Appl. Phys. Lett. **113**, 202102 (2018).
[42] Q. Liu, J. Dai, Z. Liu, X. Zhang, G. Zhu, and G. Ding, J. Phys. D.: Appl. Phys. **43**, 455401 (2010).
[43] H. J. Kim, J. Kim, T. H. Kim, W.-J. Lee, B.-G. Jeon, J.-Y. Park, W. S. Choi, D. W. Jeong, S. H. Lee, J. Yu, T. W. Noh, and K. H. Kim, Phys. Rev. B **88**, 125204 (2013).
[44] H. Mizoguchi, P. Chen, P. Boolchand, V. Ksenofontov, C. Felser, P. W. Barnes, and P. M. Woodward, Chem. Mater. **25**, 3858 (2013).
[45] U. Kim, C. Park, T. Ha, R. Kim, H. S. Mun, H. M. Kim, H. J. Kim, T. H. Kim, N. Kim, J. Yu, K. H. Kim, J. H. Kim, and K. Char, APL Mater. **2**, 056107 (2014).
[46] K. Ganguly, P. Ambwani, P. Xu, J. S. Jeong, K. A. Mkhoyan, C. Leighton, and B. Jalan, APL Mater. **3**, 062509 (2015).
[47] H. M. I. Jaim, S. Lee, X. Zhang, and I. Takeuchi, Appl. Phys. Lett. **111**, 172102 (2017).
[48] H.-R. Liu, J.-H. Yang, H. J. Xiang, X. G. Gong, and S.-H. Wei, Appl. Phys. Lett. **102**, 112109 (2013).
[49] S. Dabaghmanesh, R. Saniz, M. N. Amini, D. Lamoen, and B. Partoens, J. Phys.: Condens. Matter **25**, 415503 (2013).
[50] D. O. Scanlon, Phys. Rev. B **87**, 161201(R) (2013).
[51] D. J. Singh, Q. Xu, and K. P. Ong, Appl. Phys. Lett. **104**, 011910 (2014).
[52] K. Krishnaswamy, B. Himmetoglu, Y. Kang, A. Janotti, and C. G. Van De Walle, Phys. Rev. B **95**, 205202 (2017).
[53] P. Singh, B. J. Brandenburg, C. P. Sebastian, P. Singh, S. Singh, D. Kumar, and O. Parkash, Jpn. J. Appl. Phys. **47**, 3540 (2008).
[54] T. N. Stanislavchuk, A. A. Sirenko, A. P. Litvinchuk, X. Luo, and S.-W. Cheong, J. Appl. Phys. **112**, 044108 (2012).
[55] W. Nunn, A. Prakash, A. Bhowmik, R. Haislmaier, J. Yue, J. M. Garcia Lastra, and B. Jalan, APL Mater. **6**, 066107 (2018).
[56] K. Fujiwara, K. Nishihara, J. Shiogai, and A. Tsukazaki, Appl. Phys. Lett. **110**, 203503 (2017).
[57] A. Prakash, J. Dewey, H. Yun, J. S. Jeong, K. A. Mkhoyan, and B. Jalan, J. Vac. Sci. Technol. A **33**, 060608 (2015).
[58] H. Wang, A. Prakash, K. Reich, K. Ganguly, B. Jalan, and C. Leighton, APL Mater. **8**, 071113 (2020).
[59] B. Luo and J. Hu, ACS Appl. Electron. Mater. **1**, 51 (2019).
[60] H. Yun, K. Ganguly, W. Postiglione, B. Jalan, C. Leighton, K. A. Mkhoyan, and J. S. Jeong, Sci. Rep. **8**, 10245 (2018).
[61] W. Y. Wang, Y. L. Tang, Y. L. Zhu, J. Suriyaprakash, Y. B. Xu, Y. Liu, B. Gao, S. W. Cheong, and X. L. Ma, Sci. Rep. **5**, 16097 (2015).
[62] L. Weston, L. Bjaalie, K. Krishnaswamy, and C. G. Van De Walle, Phys. Rev. B **97**, 054112 (2018).
[63] A. Prakash and B. Jalan, Adv. Mater. Interfaces **6**, 1900479 (2019).
[64] R. Uecker, R. Bertram, M. Brützam, Z. Galazka, T. M. Gesing, C. Guguschev, D. Klimm, M. Klupsch, A. Kwasniewski, and D. G. Schlom, J. Cryst. Growth **457**, 137 (2017).
[65] C. Guguschev, D. Klimm, M. Brützam, T. M. Gesing, M. Gogolin, H. Paik, A. Dittmar, V. J. Fratello, and D. G. Schlom, J. Cryst. Growth **528**, 125263 (2019).
[66] M. Ohring, *Materials Science of Thin Films*, 2nd ed. (Academic, San Diego, 2002).
[67] U. Poppe, N. Klein, U. Dähne, H. Soltner, C. L. Jia, B. Kabius, K. Urban, A. Lubig, K. Schmidt, S. Hensen, S. Orback, G. Muller, and H. Piel, J. Appl. Phys. **71**, 5572 (1992).
[68] C. L. Jia, M. I. Faley, U. Poppe, and K. Urban, Appl. Phys. Lett. **67**, 3635 (1995).
[69] M. Varela, D. Arias, Z. Sefrioui, C. León, C. Ballesteros, and J. Santamaria, Phys. Rev. B **62**, 12509 (2000).
[70] M. Varela, W. Grogger, D. Arias, Z. Sefrioui, C. León, C. Ballesteros, K. M. Krishnan, and J. Santamaria, Phys. Rev. Lett. **86**, 5156 (2001).
[71] Z. Sefrioui, D. Arias, V. Peña, J. E. Villegas, M. Varela, P. Prieto, C. León, J. L. Martinez, and J. Santamaria, Phys. Rev. B **67**, 214511 (2003).
[72] J. Garcia-Barriocanal, F. Y. Bruno, A. Rivera-Calzada, Z. Sefrioui, N. M. Nemes, M. Garcia-Hernández, J. Rubio-Zuazo, G. R. Castro, M. Varela, S. J. Pennycook, C. Leon, and J. Santamaria, Adv. Mater. **22**, 627 (2010).
[73] F. Y. Bruno, J. Garcia-Barriocanal, M. Varela, N. M. Nemes, P. Thakur, J. C. Cezar, N. B. Brookes, A. Rivera-Calzada, M. Garcia-Hernandez, C. Leon, S. Okamoto, S. J. Pennycook, and J. Santamaria, Phys. Rev. Lett. **106**, 147205 (2011).
[74] J. Walter, T. Charlton, H. Ambaye, M. R. Fitzsimmons, P. P. Orth, R. M. Fernandes, and C. Leighton, Phys. Rev. Mater. **2**, 111406(R) (2018).
[75] J. Walter, S. Bose, M. Cabero, G. Yu, M. Greven, M. Varela, and C. Leighton, Phys. Rev. Materials **2**, 111404(R) (2018).
[76] J. Walter, S. Bose, M. Cabero, M. Varela, and C. Leighton, Phys. Rev. Materials **4**, 091401(R) (2020).
[77] P. Ambwani, P. Xu, G. Haugstad, J. S. Jeong, R. Deng, K. A. Mkhoyan, B. Jalan, and C. Leighton, J. Appl. Phys. **120**, 055704 (2016).

[78] R. F. Egerton, *Electron Energy-Loss Spectroscopy in the Electron Microscope*, 3rd ed. (Springer, New York, 2011).

[79] K. Ganguly, W. Postiglione, L. Borgeson, A. Prakash, H. Yun, J. S. Jeong, K. A. Mkhoyan, B. Yang, A. M. Goldman, B. Jalan, and C. Leighton, Unpublished, (2018).

[80] See Supplemental Material at http://link.aps.org/supplemental/10.1103/PhysRevMaterials.5.044604 for additional atomic force microscopy imaging, reciprocal space map characterization, thickness-dependent data at low deposition rate, reciprocal space mapping before and after annealing, lightly-doped buffer layer electrical characterization, and temperature-dependent transport on the highest mobility film in this study.

[81] M. Sharma, J. Gazquez, M. Varela, J. Schmitt, and C. Leighton, J. Vac. Sci. Technol. A **29**, 051511 (2011).

[82] Z. Zhang, W. Sigle, W. Kurtz, and M. Rühle, Phys. Rev. B **66**, 214112 (2002).

[83] A. Spinelli, M. A. Torija, C. Liu, C. Jan, and C. Leighton, Phys. Rev. B **81**, 155110 (2010).

[84] E. H. Smith, P. D. C. King, A. Soukiassian, D. G. Ast, and D. G. Schlom, Appl. Phys. Lett. **111**, 131903 (2017).